Molecular Systems Biology 7; Article number 519; doi:10.1038/msb.2011.49
Citation: *Molecular Systems Biology* 7:519

www.molecularsystemsbiology.com

molecular systems biology

Synthetic incoherent feedforward circuits show adaptation to the amount of their genetic template

Leonidas Bleris[1], Zhen Xie[2], David Glass[3], Asa Adadey[4], Eduardo Sontag[5] and Yaakov Benenson[6,*]

[1] Department of Bioengineering and Department of Electrical Engineering, University of Texas at Dallas, Richardson, TX, USA, [2] Department of Biological Engineering, Massachusetts Institute of Technology, Cambridge, MA, USA, [3] Princeton University, Princeton, NJ, USA, [4] University of Maryland Baltimore County, Baltimore, MD, USA, [5] Department of Mathematics, Rutgers—The State University of New Jersey Hill Center, Piscataway, NJ, USA and [6] Department of Biosystems Science and Engineering, Eidgenössische Technische Hochschule (ETH Zürich), Basel, Switzerland

* Corresponding author. Department of Biosystems Science and Engineering, Eidgenössische Technische Hochschule (ETH Zürich), Mattenstrasse 26, 4058 Basel, Switzerland. Tel.: +41 61 387 3338; Fax: +41 61 387 3994; E-mail: kobi.benenson@bsse.ethz.ch

Received 13.12.10; accepted 6.6.11

Natural and synthetic biological networks must function reliably in the face of fluctuating stoichiometry of their molecular components. These fluctuations are caused in part by changes in relative expression efficiency and the DNA template amount of the network-coding genes. Gene product levels could potentially be decoupled from these changes via built-in adaptation mechanisms, thereby boosting network reliability. Here, we show that a mechanism based on an incoherent feedforward motif enables adaptive gene expression in mammalian cells. We modeled, synthesized, and tested transcriptional and post-transcriptional incoherent loops and found that in all cases the gene product adapts to changes in DNA template abundance. We also observed that the post-transcriptional form results in superior adaptation behavior, higher absolute expression levels, and lower intrinsic fluctuations. Our results support a previously hypothesized endogenous role in gene dosage compensation for such motifs and suggest that their incorporation in synthetic networks will improve their robustness and reliability.
Molecular Systems Biology **7**: 519; published online 2 August 2011; doi:10.1038/msb.2011.49
Subject Categories: metabolic and regulatory networks; synthetic biology
Keywords: feedforward motifs; gene dosage and noise; mammalian cells; microRNAs; negative autoregulation

Introduction

Biological networks typically contain small-scale subnetworks of recurring topology called 'motifs' (Milo *et al*, 2002; Balazsi *et al*, 2005; Ma'ayan *et al*, 2005). The most common motifs are feedforward and feedback (autoregulatory) loops (Shen-Orr *et al*, 2002), with the former being largely dominated by an 'incoherent' connectivity (Mangan and Alon, 2003) in bacteria (Mangan *et al*, 2006) and yeast (Lee *et al*, 2002). Incoherent feedforward motifs were also observed in mammalian cells (Boyer *et al*, 2005), although to the best of our knowledge their prominence remains to be determined. The canonical three-node incoherent loop contains input, auxiliary regulator, and output nodes. The output is controlled directly by the input and the auxiliary regulator. The latter is also controlled by the input, introducing an additional indirect effect of the input on the output. In incoherent loops, the input controls the auxiliary regulator node in such a way that input's overall indirect action on the output via this node counteracts its direct effect. In a motif named 'type I incoherent feedforward loop' (I1-FFL), the input's direct effect is activating, as is its control of the auxiliary node, while the auxiliary node controls the output through repression. Because this motif comprises about 30% of all three-node interaction loops in transcriptional circuits (Mangan *et al*, 2006), a number of studies have attempted to uncover the reasons behind its prevalence by artificially creating plausible operating scenarios and testing whether the topology is superior to alternative arrangements.

One line of research studied transcription factor (TF)-based motifs by experimentally perturbing small molecule TF cofactors. Using this setup, a synthetic incoherent motif was shown to act as pulse generator in cell communication experiments (Basu *et al*, 2004), while in another study (Mangan *et al*, 2006) a naturally occurring motif embedded in a galactose utilization pathway produced a faster response to its cognate environmental signal compared with the baseline. Other studies showed that steady-state output levels peak at an intermediate input level, generating a non-monotonic transfer function in synthetic (Entus *et al*, 2007) and natural (Kaplan *et al*, 2008) systems. Recently, the topology has been shown to enable a 'fold-change' detection in the strength of the input signal when the intensity of the transient response was used as output (Goentoro *et al*, 2009) (provided that certain scaling transformations preserve the form of the system (Shoval *et al*, 2010)) and to possess a type of 'memory' effect of the intensity of previously seen step signals (Sontag, 2010).

Enzyme-based incoherent motifs were identified and classified in a study that sought adaptive properties in a computationally generated library of network topologies in signaling pathways (Ma *et al*, 2009). In such a motif, enzyme A (input) activates enzyme C (output) as well as enzyme B (auxiliary regulator) that in turn inactivates enzyme C. The enzymatic circuit functions as a pulse generator, similarly to its transcriptional counterpart. Similar architectures had been devised earlier from first principles (Tyson *et al*, 2003) and analyzed from a theoretical standpoint (Sontag, 2010). Finally, it was mathematically shown that two-component genetic circuits with elements of opposite regulatory activity constitute the minimal requirement for network-dosage invariance (Acar *et al*, 2010).

We propose a novel implementation of the I1-FFL, where the input (black circle in Figure 1A) is a DNA fragment coding for

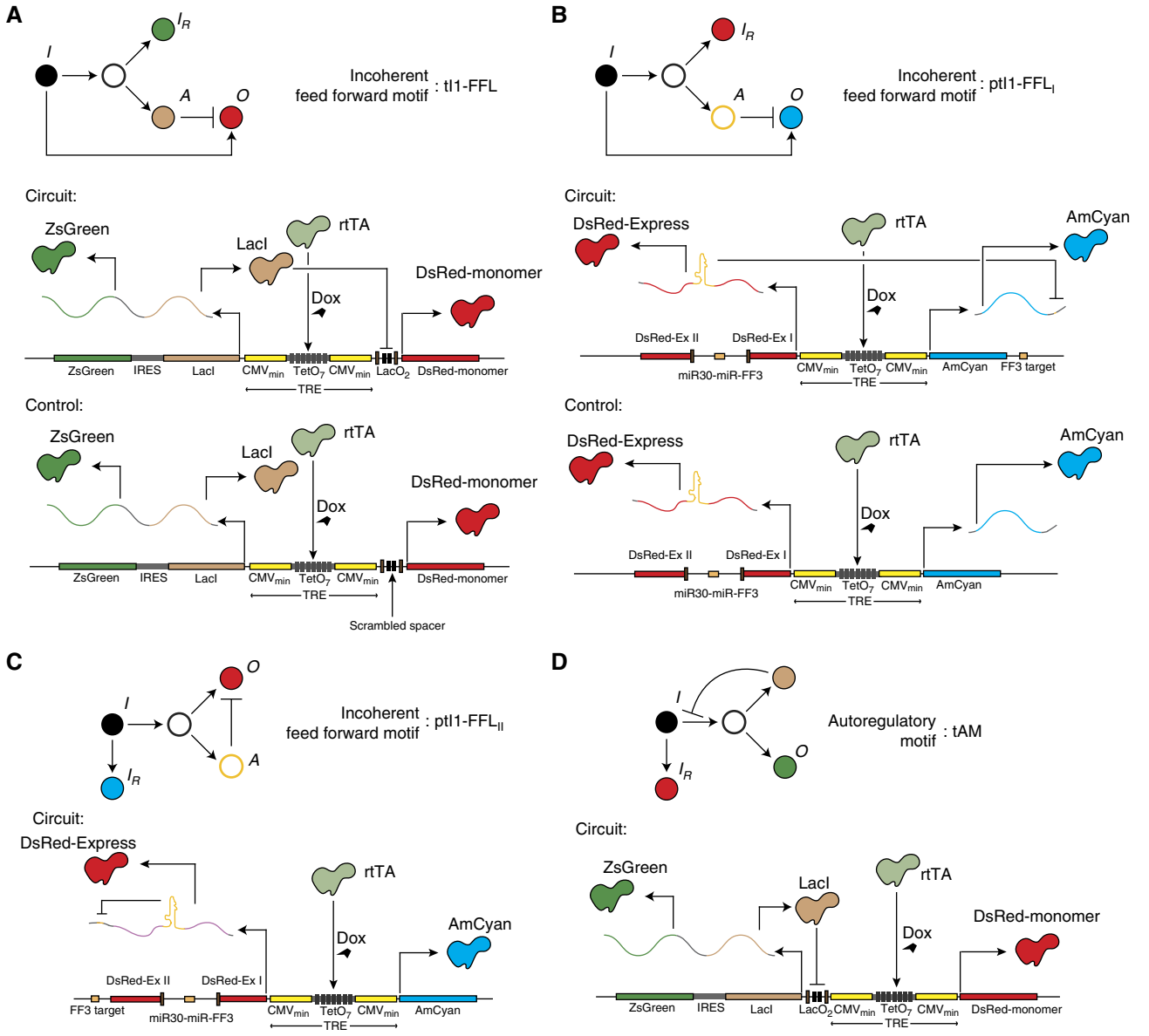

Figure 1 Schematics of the synthetic networks. Pointed and blunt arrows denote activation and repression, respectively. In all constructs, the output protein and the repressor are transcribed from the same bidirectional promoter in the constant and non-limiting presence of the TF rtTA that does not constitute an input to the system. In the diagrams, *I* indicates input node, I_R is the input reporter, *A* is the auxiliary regulator, and *O* is the output. (**A**) Transcriptional type I incoherent feedforward motif (tI1-FFL): the output protein is DsRed and the auxiliary repressor is LacI. The plasmid copy number is reported by the ZsGreen1 fluorescent protein, cotranslated with the LacI protein using IRES. Corresponding control circuit is also shown. (**B**) Post-transcriptional type I incoherent feedforward motif version I (ptI1-FFL$_I$): the output protein is AmCyan and the auxiliary repressor is a microRNA. Plasmid copy number is reported by the DsRed protein coexpressed with the output. DsRed mRNA also contains an intron coding for the regulator microRNA. Corresponding control circuit is also shown. (**C**) Post-transcriptional type I incoherent feedforward motif version II (ptI1-FFL$_{II}$): the output protein is DsRed, repressed by a microRNA processed from the intron in its own mRNA. The input is reported by the divergently expressed AmCyan protein. The control circuit is identical to the one in (B). (**D**) Transcriptional negative autoregulation motif (tAM): auxiliary repressor LacI becomes the output and represses its own transcription as well as the level of the ZsGreen output reporter contranslated via IRES. The input is reported by a divergently expressed DsRed protein.

both the auxiliary regulator (brown circle) and the output (red circle), with the regulator negatively affecting the output. We might expect the transient and steady-state input–output relation of our circuits to be similar to those of the previously described systems. However, while enzymatic or TF inputs can be experimentally modulated in single cells in a temporal manner, it is not so with DNA inputs. Therefore, our main interest lies in the steady-state relation between the amount of DNA template and the amount of the output protein. Aforementioned studies showed pulse-like output response, or output adaptation, to abrupt temporal changes in the input, meaning that different input levels generate the same output in the steady state. This leads to a conjecture that in our circuits, the steady-state output levels will not depend on the number of DNA molecules that code for the circuit, a property we also call adaptation. An affirmative answer to this conjecture would add experimental support to the hypothesis (Veitia *et al*, 2008) that similar circuitry might be employed by cells to implement gene dosage compensation in the context of neuronal homeostasis (Tsang *et al*, 2007), sex determination (Lucchesi *et al*, 2005), and ploidy changes. It would also suggest that such circuits could become valuable tools (Holtz and Keasling, 2010) in the construction of increasingly complex synthetic networks (Russell and Aloy, 2008; Cantone *et al*, 2009; Lu *et al*, 2009) because they will contribute to overall robustness of the system by decreasing natural variability in the circuits' components.

We tested our circuits in mammalian cells, motivated by their potential relevance to eukaryotic dosage compensation and to mammalian synthetic biology, and in order to explore RNA interference (RNAi) as a negative regulation mechanism. We compared them to a negative autoregulatory motif (Becskei and Serrano, 2000; Isaacs *et al*, 2003) that had been shown in bacteria to weaken the dependency of the expression level on DNA template amount as well as to reduce protein expression fluctuation.

Results

Study rationale and circuit details

In order to explore the input–output behavior of any given system, and specifically adaptation, one needs to generate a wide range of input values and measure the corresponding outputs. Here, to test our hypothesis regarding I1-FFL adaptation to copy number, we relied on transient transfection of DNA plasmids into mammalian cells that generates large variability in the number of plasmids internalized by individual cells. Single plasmids were used to encode all circuit components in order to minimize irrelevant fluctuations typical of plasmid cotransfection. The circuit's input, that is, the number of plasmid copies in a cell, is determined using a constitutively expressed fluorescent protein. Published literature generally supports the view that in transient transfections, fluorescence depends linearly on the copy number of transfected plasmids (Tseng *et al*, 1997; Pollard *et al*, 1998; Cohen *et al*, 2009; Schwake *et al*, 2010); in addition, we verified this assertion experimentally as shown below. While strictly speaking, this reporter level also depends on many other potentially fluctuating parameters such as global synthesis and degradation rates, it is the differences in the copy number that are the major source of cell-to-cell variability in transient transfections. Therefore, as a first approximation, the copy number is considered as the sole contributor to the differences in reporter levels. Another fluorescent protein, whose expression is controlled by the input and the auxiliary regulator, serves as the output.

We considered three motif variants to test the effect of both transcriptional and post-transcriptional repression by the auxiliary node (Figure 1A–C). In the first variant, a transcriptional repressor LacI coexpressed with the DsRed-monomer output downregulates this output via binding to LacO operator in its promoter, implementing a transcriptional tI1-FFL (Figure 1A). Four LacO mutants are used to quantify the effect of weakened LacI binding on circuit performance, while the plasmid copy number is judged by the level of ZsGreen1 fluorescent reporter that is cotranslated with LacI using an internal ribosome entry site (IRES). Control circuit for this motif contains fully scrambled spacer instead of LacO-binding site. In the second variant, a post-transcriptional type I incoherent feedforward motif version I (ptI1-FFL$_{I}$; Figure 1B), the auxiliary regulator is a synthetic microRNA (miR-FF3) that targets a complementary RNA sequence fused into the 3′-UTR of the output AmCyan mRNA (Rinaudo *et al*, 2007). miR-FF3 is processed post-splicing from an intron (Leisner *et al*, 2010) inserted between two exons coding for a fluorescent protein DsRed-Express. Corresponding control circuit does not contain a target site for miR-FF3, eliminating the RNAi against AmCyan. The third variant of an incoherent motif uses a negative miR regulator that is processed from an intron fused into a protein-coding mRNA; the miR then downregulates this mRNA post-splicing (Figure 1C). This post-transcriptional I1-FFL version II (ptI1-FFL$_{II}$) utilizes the same DsRed–miR-FF3 fusion construct as ptI1-FFL$_{I}$ but this time the FF3 target is inserted into 3′-UTR of DsRed mRNA itself. In this particular topology, unspliced RNA that is the input for the motif generates the output mRNA as well as the miR regulator of this output. If the regulator acted on the unspliced RNA molecule then the topology would become that of negative autoregulation, but that is not the case here, as the splicing is completed before the miR enters the RNAi pathway. The AmCyan fluorescent protein, divergently expressed from a pTRE promoter, serves as a copy number reporter. Control construct for this last motif is identical to the one used for version I circuit, because RNAi against DsRed is non-functional due to the absence of miR-FF3 target in DsRed 3′-UTR.

We compare the behavior of our circuits with the well-studied negative feedback motif (Figure 1D). This transcriptional autoregulatory motif (tAM) was constructed by inverting the promoter region of the tI1-FFL, thus placing the LacO sequences in front of the LacI-coding frame. As a result, the LacI protein represses the transcription of its own mRNA, and the circuit's output is now reflected in the level of ZsGreen1 reporter, while the copy number is judged based on the divergently expressed DsRed protein.

Modeling of input–output relation

We preceded our experiments with mathematical modeling and computer simulations in order to gain insight into circuits'

qualitative behavior (for details, see Supplementary Information). First, we ran numerical simulations using the Matlab SimBiology toolbox. Second, we derived a set of ordinary differential equations based on our current mechanistic understanding of individual interactions in the motifs, and studied the circuits analytically. Numerical simulations show that the output of all incoherent motifs adapts to copy number changes (Figure 2A and B) and the input–output response is well fitted by a 'rational function' (Supplementary Figure S1A and B; Supplementary Table S1), where the nominator and the denominator are first-degree polynomials. Weaker inhibition results in slower adaptation, eventually leading to a linear input–output mapping. This is manifested by the gradual increase in EC_{50} values, that is, input values at which the output reaches half of its saturated value (Figure 2C and D).

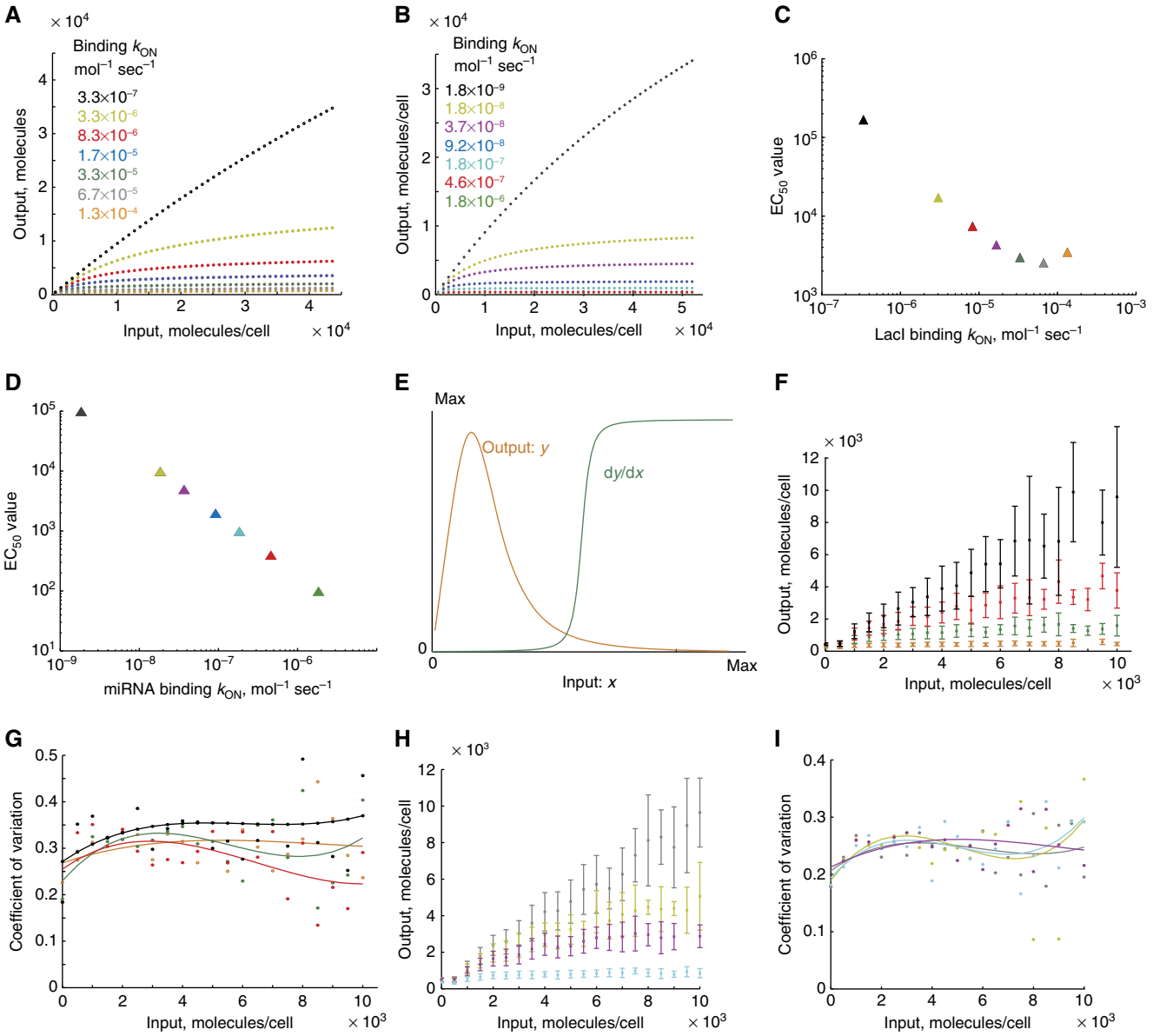

Figure 2 Simulations for the transcriptional and post-transcriptional (ptI1-FFL$_I$) type I incoherent feedforward motif. (**A**) Noise-free parametric simulations of the tI1-FFL with increasing binding strength of the LacI inhibition, from weak inhibition case (black curve) to strong inhibition (orange curve). Binding rate constants in 1/(mol*sec) units used to generate the different curves are similarly color coded. (**B**) Noise-free parametric simulations of the ptI1-FFL$_I$ with increasing efficiency of the miRNA inhibition, from weak inhibition (gray curve) to strong inhibition (green curve). Identically color-coded binding rate constant values are shown in 1/(mol*sec) units. (**C**) Fitted EC_{50} values of the simulated tI1-FFL response for the binding rate constants in panel (A). (**D**) Fitted EC_{50} values of the simulated ptI1-FFL$_I$ response for the binding rate constants in panel (B). (**E**) Two special cases in circuits' response. The orange curve shows a biphasic input–output behavior of the tI1-FFL, while the green curve shows the first derivative of the output in ptI1-FFL$_I$ consistent with the transition from a saturated to a proportional response. (**F**) Noisy simulations of the tI1-FFL for increasing binding of the LacI. The colors correspond to the LacI-binding rate constants in panel (A). (**G**) The coefficients of variation obtained in the noisy simulations of tI1-FFL. The colors correspond to the LacI-binding rate constants of panel (A). (**H**) Noisy simulations of the ptI1-FFL$_I$ for increasing strength of the miRNA binding. The colors correspond to the binding rate constants in panel (B). (**I**) Coefficients of variation of the noisy simulations of the ptI1-FFL$_I$. The colors correspond to the miRNA-binding rate constants of panel (B).

The qualitative ODE analysis (Supplementary Figure S6) reproduced numerical simulations and provided important additional information about the system. We found that when LacI di- and tetramerization are very fast and essentially irreversible resulting in no detectable degradation of LacI monomers and dimers, and LacI tetramer degradation rate is low, the output (y) depends on the input (x) according to the following Michaelis–Menten form

$$y = \frac{Vx}{1 + Kx}$$

for positive constants V and K, where the constant K is directly proportional to the strength of LacI binding to the LacO operator. In the unrepressed case (K=0), y is simply proportional to x. As a way to model a non-zero mean value of the output when the copy number is zero (important when fitting flow cytometry data), we modify the above formula to the more general form

$$y = \frac{Vx + W}{1 + Kx}$$

or, using different parameterization,

$$y = \sigma(x) = c\frac{x + a}{x + b}$$

We observe that all the above formulas belong to the category of rational functions that exhibit saturating behavior in agreement with our numerical simulations. When no assumptions are made regarding LacI multi-merization, while still assuming that the degradation of the LacI species is very slow, we obtain

$$y = \frac{Vx}{1 + Kx^4}$$

Note that this is a 'biphasic' function that increases from zero to some maximal value and then decreases to zero (Figure 2E, orange curve).

We next analyzed the model of the ptI1-FFL$_I$ circuit, and again concluded that the output saturates with increasing input. However, for high copy numbers and low concentrations of RNA-induced silencing complex (RISC), we observe that an increase in the copy number does not lead to an increase in the feedforward inhibition due to saturation of RISC, resulting in the loss of adaptive behavior. We plot a derivative dy/dx of this response (Figure 2E, green curve) with low derivative values at low input values characteristic of adaptation, and high values at high input values indicating linear dependency.

Modeling of noisy data

Next, we attempted to generate *in silico* flow cytometry data likely to be obtained in transient transfections by executing the code multiple times, each time corresponding to a single-cell readout. The consecutive runs differed in their initial conditions and the parameter values in order to reflect copy number variability between different cells in transient transfection as well as fluctuations in individual cells (i.e. intrinsic noise). Since the values for neither variability nor fluctuations can be obtained from first principles, we measured them in a number of control experiments. First, copy number distribution was measured using transiently transfected ZsGreen1-encoding plasmid. The amplitude of the measured fluorescence was assigned to correspond to 100 plasmid copies based on our experimental estimation (see below), and the distribution redrawn in copy number units assuming linear relationship between the fluorescence and the copy number (see below). Plasmid copy number was then picked randomly from that distribution and used as an initial condition for each code execution (Supplementary Figure S1C and D).

Second, we experimentally measured intrinsic noise in certain components of our system, that is, fluctuations in the relative protein amounts generated from the same DNA template. Two easily identifiable sources of fluctuations are coexpression from the bidirectional promoter and cotranslation from a bicistronic mRNA. In addition, one could expect fluctuations in the negative regulation step by an auxiliary node, meaning that for given steady-state levels of the regulator (e.g. LacI) and its target (e.g. pTRE-LacO-DsRed) the output (e.g. DsRed) levels in different cells will change stochastically due to uncertainty in the exact amount of active and inactive (e.g. bound to LacI) targets. These noisy steps combine to determine the distribution of the output values for a given input reporter value in our circuits. Fluctuations in the bidirectional promoter were measured by coexpressing AmCyan and DsRed from pTRE-Tight promoter (Supplementary Figure S1E); fluctuations in cotranslation were measured by coexpressing DsRed and ZsGreen from a bicistronic mRNA (Supplementary Figure S1F) driven by a constitutive CMV promoter.

The data were used to randomize parameter values and simulate a set of stochastic single-cell readouts. Those readouts are then processed as follows: (1) the range of input values is divided into a number of bins of equal width; (2) all 'cells' whose simulated input values fall into a particular bin are collected together and assumed to have the same input value, corresponding to the center of a bin; (3) the mean output values of these cells and the coefficient of variance (CV) of these values are used to determine, respectively, the mean circuit response and its intrinsic noise for this input. We apply the same procedure to the experimental data (Supplementary Figure S2A–D).

As shown in Supplementary Figure S1H, the CV is $\sim$0.25 for the bidirectional promoter and $\sim$0.3 for the IRES. When plugged into the simulation of tI1-FFL (Figure 2F and G), these values generate $\sim$0.35 variability in the negative control circuit variant without a functional LacO site, and the variability decreases slightly to $\sim$0.3 when we turn on LacI repression. However, experimental measurement of the negative control circuit showed variability of $\sim$0.55 (Supplementary Figure S1G and H), indicating that there are additional noise sources even in the absence of negative regulation. One possible reason for this increase is pTRE promoter symmetry breaking with a spacer. Similarly, we simulated ptI1-FFL$_I$ taking into account bidirectional promoter noise. We predict CV of $\sim$0.25 variability regardless of miR efficiency (Figure 2H and I), which compares to the observed CV of $\sim$0.5 in the negative control circuit. Here, the extra noise could arise from the asymmetry introduced by splicing in one of the transcripts, but not the other.

Experimental characterization

We commenced our experiments with testing data reproducibility by comparing the mean output values and their fluctuations measured under various conditions. The averaged input–output function of the tI1-FFL and the noise levels exhibit the following characteristics: (1) they are insensitive to changes in plasmid amounts used in transfections as well as Dox levels (Supplementary Figure S2E–K); (2) that are slightly sensitive to changes in transfection reagent (Supplementary Figure S2L and M); and (3) they do not change between 48 and 72 h post-transfection (Supplementary Figure S2N and O). The latter result suggests that the system is in a quasi-steady state during this time window, even though transient transfections result in eventual loss of plasmids from the cells. Unlike the transcriptional circuit, ptI1-FFL$_I$ reaches different saturated levels and exhibits different intrinsic noise (Supplementary Figure S3A and B) depending on the DNA amount and the reagent. However, these responses were reproducible for a given combination of both (Supplementary Figure S3C–F). We were not able to atribute this to any single experimental parameter and hypothesize that it is related to global changes in RNAi pathway activity in the cells that might be affected by transfection conditions. After initial calibration, we collected data from all circuit variants using 500 ng of the plasmids and LipoLTX transfection reagent. We note that in order to compare different circuits that used different fluorescent proteins to report on input and output values, we normalized the raw values obtained in FACS measurements to those from the tI1-FFL negative control circuit so that the data from the respective negative control constructs used for different circuit families would all overlap post-normalization (Supplementary Figure S3G and H). Additionally, in our processing of the flow cytometry data, we restricted our analysis to those bins whose mean output value is less than half the dynamic range of the instrument (125 000 units) in order to avoid biased calculations of mean and s.d. by including saturated data points (data not shown).

First, we transfected transcriptional incoherent motifs with varying LacO sites (Figure 3A, C, and D). Qualitatively, one observes that the response becomes less dependent on the copy number as the binding strength increases, but it never

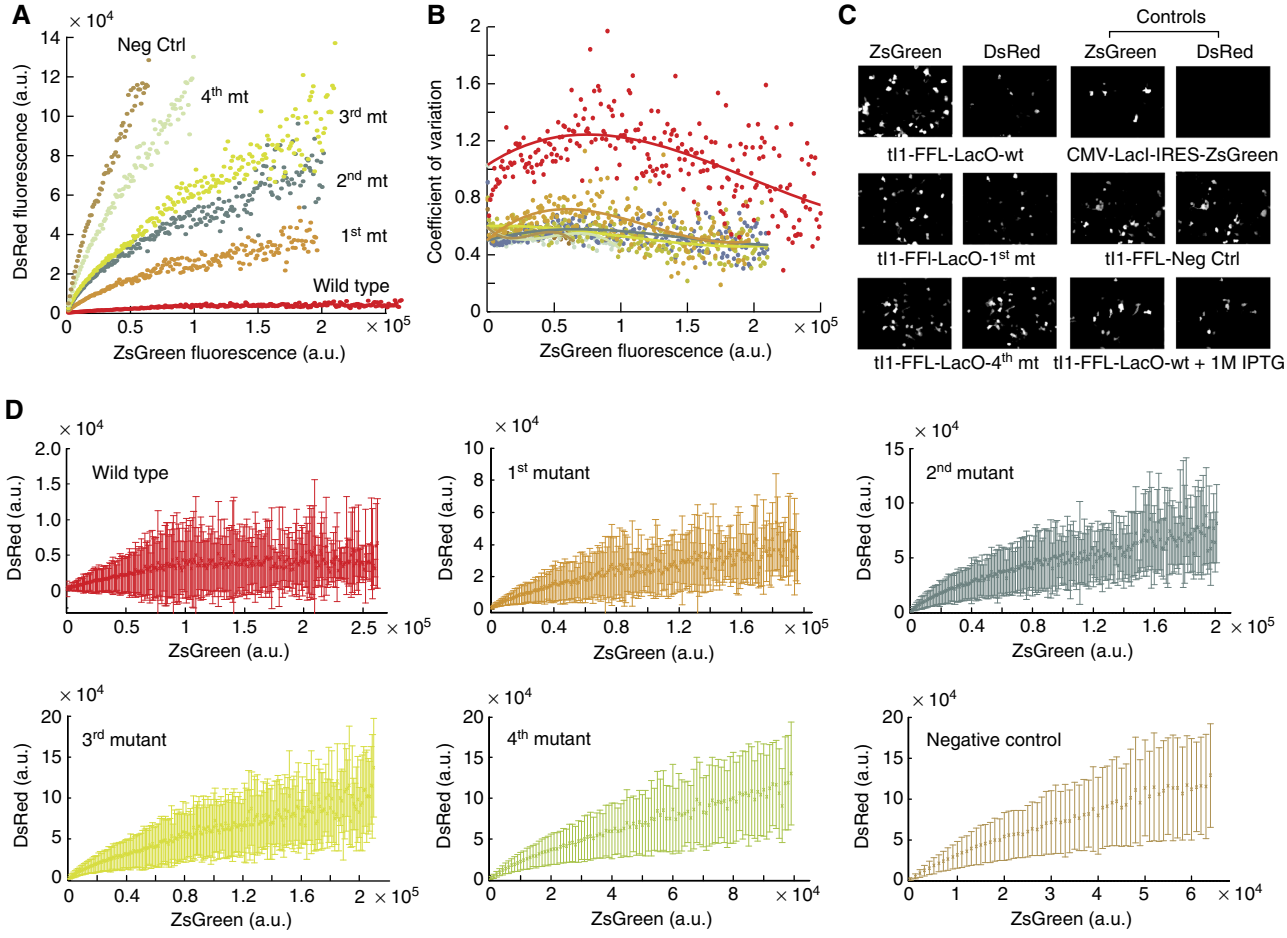

Figure 3 Experimental results with tI1-FFL motifs. Microscopy images are used for illustration, accompanied by the quantitative data obtained from flow cytometry analysis of at least 200 000 cells from each transfected well. (**A**) Experimentally measured input–output response of tI1-FFL. Red curve corresponds to wild-type LacO; orange, dark cyan, green, and light green curves represent four mutants with gradually decreasing LacI binding; brown curve is the negative control. (**B**) Coefficient of variation for each of the constructs illustrated in panel (A) using identical color coding. (**C**) Representative microscopy images of the circuits and controls. (**D**) Processed flow cytometry data measured for six tI1-FFL constructs, showing mean output values and their s.d. in each bin. Source data is available for this figure at www.nature.com/msb.

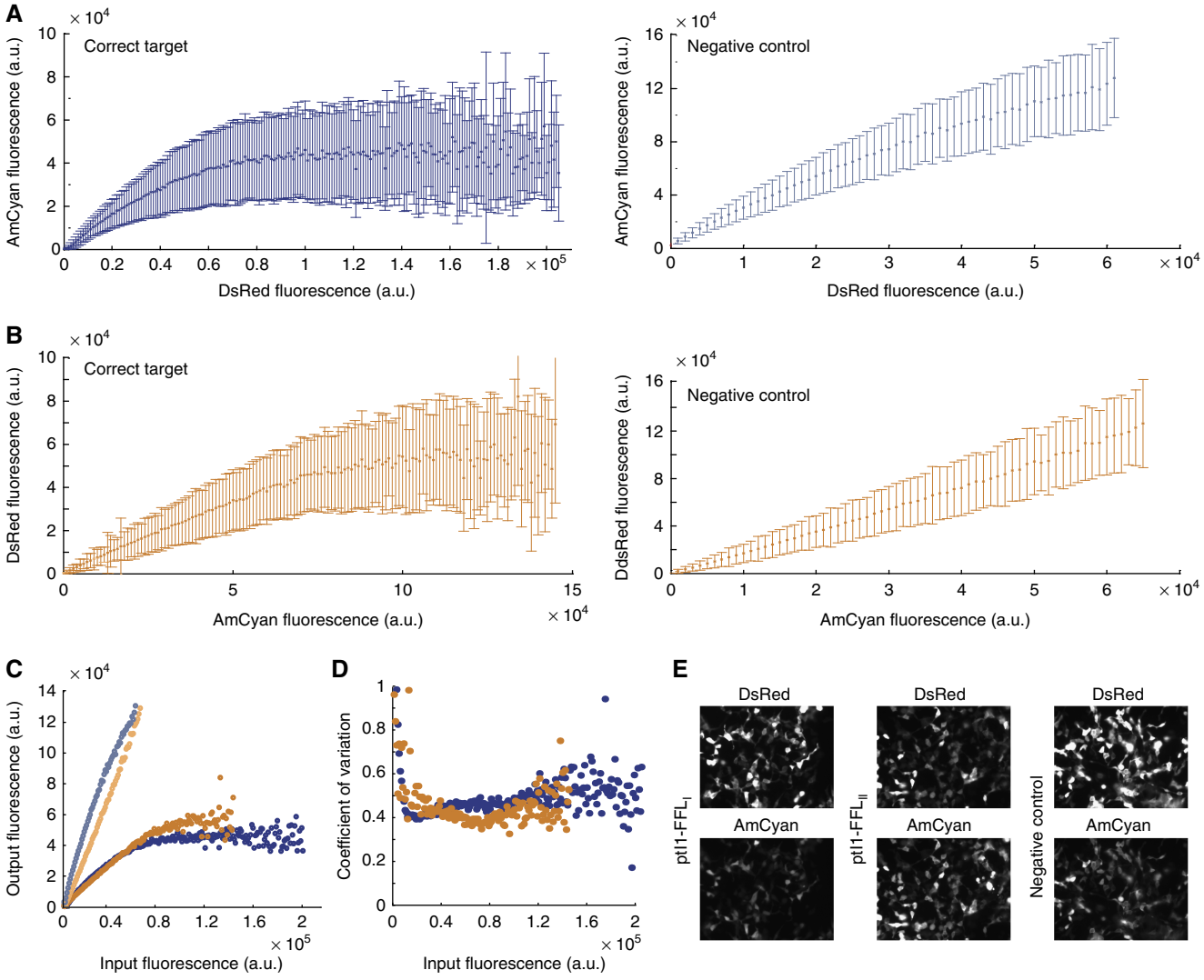

Figure 4 Experimental results obtained with ptl1-FFL$_I$ and ptl1-FFL$_{II}$ motifs. Microscopy images are used for illustration, accompanied by the quantitative data obtained from flow cytometry analysis of at least 200 000 cells from each transfected well. (**A**) ptl1-FFL$_i$; left: correct target, right: negative control, (**B**) ptl1-FFL$_{II}$; left: correct target, right: negative control, (**C**) Overlap of the input–output responses of the two versions (blue, ptl1-FFL$_I$ and orange, ptl1-FFL$_{II}$). (**D**) Coefficients of variation of the two motifs (blue, ptl1-FFL$_I$ and orange, ptl1-FFL$_{II}$). (**E**) Representative microscopy images. Source data is available for this figure at www.nature.com/msb.

becomes strictly saturated. The intrinsic noise (Figure 3B) appears to decrease with increasing copy number and is directly proportional to the strength of the LacI inhibition, indicating that extra variability is introduced at the binding step. We then tested the post-transcriptional feedforward loops. Version I shows excellent adaptive response to the increasing copy number of the input plasmid (Figure 4A). Version II (Figure 4B) exhibits comparable behavior, but the input values span a shorter range, limiting the sampling at the high input end. We juxtapose the two data sets in Figure 4C and observe that their outputs virtually overlap for similar input values. We also find that the absolute ouput expression levels at saturation are higher for both post-transcriptiponal circuits as compared with the trancriptional incoherent motif. At the same time, the intrinsic noise (Figure 4D) is about three times lower compared with the transcriptional circuits. Figure 4E shows representative microscopy images of the signals DsRed and AmCyan for the post-transcriptional feedforward loops versions I, II, and the negative control.

We further compared our circuits with the negative autoregulatory motif. We measured two circuit variants, the first with two repeats of the LacO site and the second with one LacO site. For a negative control, we abolished LacI binding by using IPTG (Figure 5A–C). The results qualitatively show that input dependency on the output weakens with increasing binding strength while the noise levels are above those of the post-transcriptional loops but are lower than the transcriptional ones. Quantitative analysis of all circuits' characteristics is given in the following section.

Having measured input–output behavior, we performed additional experiments to characterize the relationship between the fluorescence and plasmid copy number, and to explain observed differences in the input range between certain circuits and their corresponding controls. To address

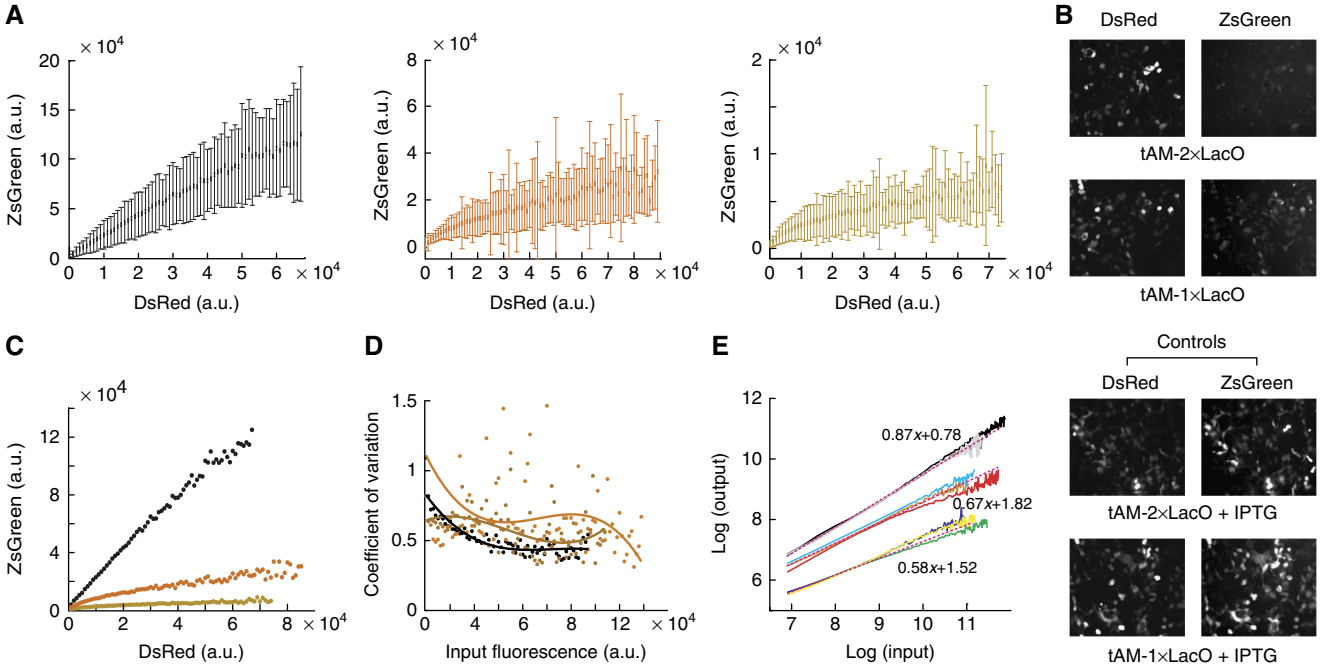

Figure 5 Experimental results obtained with tAM motifs. Microscopy images are used for illustration, accompanied by the quantitative data obtained from flow cytometry analysis of at least 200 000 cells from each transfected well. (**A**) Input–output behavior of the tAM motifs. (Left) Negative control response measured in the presence of IPTG; (middle) single LacO repeat; (right) double LacO repeat. (**B**) Representative microscopy images. (**C**) Juxtaposed mean output values obtained for the different circuits (dark gray curve: IPTG control, orange curve: single LacO repeat, light brown curve: double LacO repeat). (**D**) Coefficients of variation in the output values measured in the experiments shown in panel (A). Color coding is the same as in panel (C). (**E**) Plots of log(output) versus log(input) constructed using the mean output values measured in three replicas for each circuit variant. Source data is available for this figure at www.nature.com/msb.

the former, we sorted cells transfected with the transcriptional motif into four fractions based on input fluorescence intensity and quantitatively measured the copy number of nuclear-localized plasmids using qPCR. The results confirmed that the number of transcriptionally active plasmids depends linearly on the fluorescence intensity, with a certain threshold number of plasmids required to effect measurable gene expression (Supplementary Figure S7).

To answer the latter, we focused on the post-transcriptional ptI1-FFL$_I$, since this topology gives the largest difference between the input range in the circuit and its control. All the interactions between this circuit's components are post-transcriptional, thus it is highly unlikely that differences in the input range are due to decreased transcription rate of DsRed mRNA; instead, those differences are probably caused at the translational level. Accordingly, we conjectured that simple reduction in protein translation from AmCyan mRNA due to RNAi, rather than any topology-specific circuit feature, leads to an increase in protein translation from the DsRed mRNA and the observed increase in the input range. To test this assumption, we targeted the AmCyan mRNA in the control circuit by siRNA molecules complementary to AmCyan-coding region (Supplementary Figures S8 and S9). In Supplementary Figure S8, we show distributions of both DsRed and AmCyan markers in the circuit and the control (red and blue lines, respectively), as well as similar distributions for control circuit cotransfected with anti-AmCyan siRNA at varying concentrations. We observe that AmCyan is repressed to its levels in the functional circuit (green, orange, black, and purple data sets), while at the same time, DsRed distribution increases to circuit levels. This increase in DsRed span due to RNAi directed against the AmCyan output apparently occurs thanks to increased ribosome availability. We note that neither this increase in DsRed span nor addition of anti-AmCyan siRNA in transfection result in output adaptation to copy number (Supplementary Figure S9)

Analysis of input–output relationship

Our theoretical study showed that the exact functional form of input–output relationship should be a rational function, where the nominator and the denominator are first-degree polynomials. Therefore, we first fit the measured response to the function

$$y = \sigma(x) = c\frac{x+a}{x+b}$$

whose range is the interval $[ca/b, c]$ (we expect that ca/b will be approximately zero after fitting). The coefficient of determination (R^2) was used to quantify the goodness of fit, while the input value at which the output reaches half of its value at saturation (EC_{50}, b in the σ function) was used to rank the motifs in terms of their adaptivity. Our theoretical study predicted that stronger repression would lead to better adaptivity (smaller parameter b) and lower saturated output level compared with circuits with weak repressor binding.

Table I Goodness of fit of the data for a range of functions and EC_{50} values for the rational fit

Motif	Variant	Rational function R^2	Rational function EC_{50}	Polynomial function R^2	Linear function R^2
tI1-FFL	Wild type	0.927	53 959	0.853	0.720
tI1-FFL	Mutant 1	0.973	197 930	0.976	0.948
tI1-FFL	Mutant 2	0.975	276 860	0.9778	0.959
tI1-FFL	Mutant 3	0.988	274 860	0.988	0.968
tI1-FFL	Mutant 4	0.997	205 640	0.996	0.988
tI1-FFL	Neg. Con.	0.996	145 750	0.996	0.989
ptI1-FFL$_{I}$	FF3	0.960	27 955	0.824	0.651
ptI1-FFL$_{I}$	Neg. Con.	1.000	113 030	0.999	0.989
ptI1-FFL$_{II}$	FF3	0.981	82 128	0.963	0.905
ptI1-FFL$_{II}$	Neg. Con.	0.999	6.29×10^{15}	0.998	0.999
tAM	$2 \times$ LacO	0.963	71 764	0.970	0.941
tAM	$1 \times$ LacO	0.987	128 100	0.988	0.971
tAM	Neg. Con.	0.998	233 110	0.998	0.999

Gray shading indicates visual emphasis of different circuits.

The experimentally observed response of incoherent circuits confirmed these expectations and produced good-to-excellent fits to the rational function (Table I; Supplementary Table S2), in particular with post-transcriptional motifs. As expected, the adaptivity is reduced (EC_{50} increases) with increasing number of mutations in the LacO sites. (The absolute EC_{50} value drops again for the fourth mutant and for the negative control, but we attribute this behavior to the truncation of the cytometry data that was necessary in order to avoid using saturated measurements.) Notably, the fitted EC_{50} of the post-transcriptional motif is the lowest, confirming our qualitative observation.

We further examined the anticipated (Becskei and Serrano, 2000) square-root input–output dependency in the autoregulatory circuit. First, we observe that the log–log plot of the output versus copy number should be fitted well by a straight line whose slope is 0.5. Indeed, transformed data obtained in three independent replicas (Supplementary Figure S4A) can be fitted by a straight line (Figure 5E). Strongly repressed motif ($2 \times$ LacO) has a slope of 0.57, close to the expected value, weak inhibition ($1 \times$ LacO) results in a slope of 0.67, and the negative control experiment in 0.87 (close to the expected value of one). The slope measured for strong negative regulation agrees with previous reports. To further explain the slope values, we assume that the dynamics of the negative feedback are governed by an expression of the form

$$\dot{y} = \frac{x}{1 + Ky} - dy$$

where y is the output, x is the input, K is the strength of the negative feedback, and d is the degradation rate constant. At steady state we obtain the solution

$$y = -\frac{1}{2K} + \sqrt{\frac{1}{4K^2} + \frac{x}{dK}}$$

or

$$y = \pi_1(x) = -a + \sqrt{a^2 + bx}$$

For a very strong inhibition K, a is very small, which results in a slope of $\sim$0.5, and for a very weak inhibition, a is large, resulting in a slope of $\sim$1, which again agrees with Figure 5E. To further confirm this expectation, we fitted the motifs to π_1 and obtained excellent fit ($R^2 > 0.97$) for the autoregulatory motif (Table I; Supplementary Table S3). Finally, we replaced the exponent of 0.5 with a free parameter and fitted the motifs to the function

$$\pi_2(x) = a + (bx)^c$$

The results (Supplementary Table S4) show goodness of fit that is comparable to π_1 as exemplified by R^2, and outputs exponent values c of 0.5664, 0.6502, and 0.8490 for the $2 \times$ LacO, $1 \times$ LacO, and negative control, respectively.

We further confirmed our analysis by cross-fitting the data: the incoherent motifs were fitted to polynomial functions, while autoregulatory motifs were fitted to the above-mentioned rational function. In addition, we verified our fitting methods by checking the goodness of fit to a 'null hypothesis' described by a complete lack of adaptation, that is, a linear function. We find that in general, the incoherent motifs that implement strong inhibition by an auxiliary regulator fit well neither the polynomial nor the linear functions, confirming that indeed they exhibit saturating behavior that is not expected in the autoregulated case. The goodness of fit to the linear function (Table I; Supplementary Table S5) increases gradually for the transcriptional motif from R^2=0.72 for the wild-type LacO sequence to R^2=0.99 for the negative control, indicating progressive loss of adaptation with weakened repression efficiency. Likewise, the incoherent circuits with strong repression did not fit well to the non-saturating polynomial function, but the fit improved as the repression weakened. On the other hand, the autoregulatory motif was fit well by a rational function and considerably well by a linear function, making it hard to conclusively decide if saturation might be obtained experimentally with appropriately chosen LacI-binding sites.

Analysis of fluctuations

We analyzed the noise characteristics (Elowitz *et al*, 2002; Ozbudak *et al*, 2002; Blake *et al*, 2003; Paulsson, 2004; Raser and O'Shea, 2005; Raj *et al*, 2006; McCullagh *et al*, 2009; Kittisopikul and Suel, 2010) of different motifs, as measured by the coefficient of variation of the input values in individual bins. The transcriptional I1-FFL is significantly more noisy than the post-transcriptional implementations, resulting in CV values that range from $\sim$1.2 for low-to-medium input fluorescence to $\sim$0.9 for high input fluorescence, while the post-transcriptional I1-FFL exhibits CV of $\sim$0.45 for both implementations (Figure 4D). Post-trancriptional FFL motifs are also less noisy than the autoregulated circuits, whose noise level stands at $\sim$0.6 (exhibiting higher noise for low expression levels). The CV values compiled for all motifs are shown in Supplementary Figure S5.

Our simulations helped rationalize these observations. The control circuits allowed us to estimate individual noise contributions of certain circuit components. Using these experiments we calculated the CV of $\sim$0.25 for the bidirectional promoter, and $\sim$0.3 for IRES. These values alone would result in the total expected noise of $\sim$0.35 in the negative

control circuit (lacking LacI inhibition), with increasing the strength of the negative feedforward loop leading to reduced CV of ~0.30. However, the values observed in experiments were much higher, rising from about 0.55 in the negative control to more than 1 in fully active motifs. This shows that variability introduced by the IRES or the pTRE cannot explain the observation and leads to a hypothesis that the overall noise is dominated by the fluctuations in LacI–LacO interaction. In the case of the post-trancriptional motif, the bidirectional promoter is expected to contribute CV of ~0.25 regardless of miRNA inhibition strengths, while experimentally measured value was ~0.45 for both implementations. This suggests that there is no apparent reduction in fluctuations when the microRNA targets an mRNA spliced out of its own precursor (as in version II), compared to version I. Moreover, both the negative controls and the active circuits exhibited similar levels of fluctuation, suggesting that the discrepancy between the expected and the observed noise levels are not due to the negative regulation step but rather due to other steps in the process, such as splicing. This also suggests that RNAi inhibition is much less noisy than repression by LacI. In another interesting observation we show that the fluctuations in the autoregulated motif are not reduced as a result of the LacI binding; however, they do not increase either, as opposed to the incoherent motif. This indicates that the autoregulatory motif counteracts the increasing fluctuations of the LacI inhibition.

Discussion

We show that synthetic incoherent feedforward motifs can function as adaptive expression units in mammalian cells. Both transcriptional and post-transcriptional implementations exhibit adaptation to the amount of their genetic template, pointing to a universal property of this particular topology. The post-transcriptional RNAi-based circuits are significantly less noisy and show superior adaptability, leading to a hypothesis that nature might use such mechanisms to maintain homeostasis, filter external perturbations, and increase network robustness. Remarkably, recent studies have identified somewhat similar mechanisms of gene regulation in mammalian cells. One example, consistent with our hypothesis, is of an activator that upregulates a gene and a microRNA that then downregulates that same gene (Nakamoto *et al*, 2005; Tsang *et al*, 2007).

Our results also shed new light on the long-standing question of molecular mechanisms of gene dosage compensation. While many dosage compensation processes involve genome-wide changes, it has been hypothesized that feedback and negative feedforward effects could have a role in some cases (Tsang *et al*, 2007; Veitia *et al*, 2008; Stenberg *et al*, 2009), and mathematical analysis revealed that a two-component genetic circuit with elements of opposite regulatory activity (activator and inhibitor) constitutes a minimal requirement for network-dosage invariance (Acar *et al*, 2010). Our study shows that in fact incoherent feedforward, but not feedback, connectivity generates asymptotic response, in principle allowing dosage compensation. While qualitatively our circuits exhibit dose compensation and adaptation for increased DNA amount, the actual input values that exhibit efficient compensation are relatively high. In endogenous systems, compensation may be required when the copy number increases from two to three or two to four, or even one to two, and such compensation is unlikely to be caused by the exact replicas of our circuits. Having said that, there are examples in cancer where the amplification is eight-fold, that is, 16 copies of the gene are present in cells (Keyomarsi and Pardee, 1993), well within adaptation range in our circuits. If such dramatic amplifications are biologically feasible, the cell might pre-empt their negative effects by evolving a repressor or microRNA-binding site targeted by closely located and potentially coamplified negative regulators. In addition, future research will address the fine-tuning of the input–output response in our circuits and attempt to uncover the 'knobs' that control the half-saturation point, or EC_{50}, of the input. It is not infeasible that proper adjustments to circuit architecture could lower this value significantly in a rational manner and cause adaptive behavior even at very low copy numbers of one to four.

Finally, our study is a step toward sophisticated synthetic expression units whose gene product will depend only weakly on the number of unit copies in a cell and on global transcription and translation efficiency. Such stand-alone units, combined into larger networks, could be expected to function reliably in the face of large internal fluctuations. We note that our theoretical approach enabled us to quantitatively characterize these networks using transient transfections and noisy data; this approach eliminates the need to construct stable cell lines and dramatically reduces the time required to develop functional synthetic networks in mammalian cells.

Materials and methods

Recombinant DNA constructs

The circuits were derived from a plasmid (pTRE-Tight-Bi, Clontech), with a bidirectional pTRE-Tight promoter consisting of seven rtTA binding sites (TET_O) flanked by diverging minimal CMV promoters (CMV_{MIN}) and multiple cloning sites (MCS_I and MCS_{II}). For the cloning details see Supplemental Information, DNA Plasmids section. Using rtTA-expressing HEK293, Tet-On cells with saturating Dox concentration effectively turned pTRE-Tight into a constitutive promoter. We chose pTRE over divergently oriented pair of constitutive promoters such as CMV or UbC due to superior correlation between divergently expressed genes (data not shown).

Transfections

Approximately 120–140 thousand cells in 1 ml of complete medium were plated into each well of 12-well uncoated glass-bottom (MatTek) or plastic (Falcon) plates and grown for ~24 h. For Lipofectamine Plus transfection, mixtures were prepared by mixing all plasmids into 40 μl of Dulbecco's modified Eagle's medium (DMEM). A total of 2.4 μl of the Plus reagent (Invitrogen) was added to the final mix and incubated for 20 min at room temperature. In parallel, 1.6 μl Lipofectamine (Invitrogen) were mixed with 40 μl DMEM. Plus- and Lipofectamine-containing solutions were mixed and incubated for 20 more minutes at room temperature before application to the cells. Shortly before transfection, the medium was replaced with 1 ml DMEM without supplements with a single medium wash step. The transfection mixture (typically 90 μl) was applied to the wells and mixed with the medium by gentle shaking. Three hours after transfection, 120 μl fetal bovine serum (FBS) was added to the wells and the cells were incubated for up to 48 h before the analysis. For Lipofectamine 2000 transfections, mixtures were prepared by mixing all plasmids into

100 μl of DMEM. In parallel, 4 μl Lipofectamine 2000 (Invitrogen) were mixed with 100 μl DMEM and incubated for 5 min. Plus- and Lipofectamine 2000-containing solutions were mixed and incubated for 20 more minutes at room temperature before application to the cells. Shortly before transfection, the medium was replaced with 1 ml DMEM without supplements with a single medium wash step. The transfection mixture was applied to the wells and mixed with the medium by gentle shaking. Three hours after transfection, 120 μl FBS was added to the wells and the cells were incubated for up to 48 h before the analysis. For Lipofectamine LTX transfection, mixtures were prepared by adding each plasmids into 200 μl of DMEM. A total of 0.5 μl of the Plus reagent (Invitrogen) was added to the final mix and incubated for 5 min at room temperature. Finally, 2.5 μl Lipofectamine LTX (Invitrogen) were added. Plus- and Lipofectamine LTX-containing solutions were mixed and incubated for 30 more minutes at room temperature before application to the cells. The transfection mixture was applied to the wells and mixed with the medium by gentle shaking. The cells were incubated for up to 48 h before the analysis.

Determination of transfected plasmid copy number

For these experiments, we employed an electroporation-based method called Nucleofection using a Nucleofector 4D device (Lonza). Three million Tet-On HEK293 cells were trypsinized, spun down at 90 g for 5 min and resuspended in 200 μl of SF nucleofection medium. A total of 5 μg of PureLink (Invitrogen)-purified plasmid encoding incoherent transcriptional motif was added and the mixture split into two nucleocuvettes, about 100 μl per cuvette. The cells were nucleofected using the program CM-130 and seeded into a single T75 flask with pre-warmed growth medium pre-mixed with Dox. Cells were grown for 48 h, trypsizined, resuspended in PBS with 2 mM EDTA and sorted into four populations of varying ZsGreen intensity on a MoFlo Legacy instrument using 488 nm laser. The sorted cells as well as the unsorted population were reanalyzed on BD LRS Fortessa to confirm differential ZsGreen levels in the sorted fractions. Nuclear fraction of the sorted cells was isolated using Nuclear/Cytosol Fractionation Kit (BioVision) using provided instructions with an additional wash step of the nuclear fraction. The nuclear fraction precipitate was resuspended in PBS and DNA was extracted using DNAEasy kit (Qiagen) using the manufacturer's protocol. qPCR was performed using GoTaq qPCR master mix (Promega) using the manufacturer's instructions, with a pair of primers specific to LacI-coding region (TGCAAATGCTGAATGAGGG CATCG and ACGGCGGGATATAACATGAGCTGT) and a pair of primers specific to ACTB internal reference gene (AATGTGGCCGAGGACTTT GATTGC and AGGATGGCAAGGGACTTCCTGTAA). Calibration curves were built using known concentrations of either the transfected plasmid or subcloned ACTB cDNA (Origene). qPCR reactions were run on Lightcycler 480.

Data gathering

We transiently transfected HEK293 Tet-On cells (Clontech) using LipoLTX and assayed the output 48 h post-transfection using microscopy and flow cytometry (FACS). The small-molecule cofactor Doxycycline (Dox) was always added at saturating concentration. We used FACS data to characterize the constructs. For each cell, we measured the fluorescent intensity of the output and of the copy number reporter. The readouts ranged from 0 to about 250 000 instrument units. We sorted the cells according to their input value into equal bins of 1000 units ranging from 0 to 1000, from 1000 to 2000, etc. We then calculated the mean and the s.d. of the output levels of the cells in each bin.

Microscopy

All microscopy images were taken from live cells grown in glass-bottom wells (MatTek) in the transfection medium supplemented with 10% FBS. We used the Zeiss Axiovert 200 microscope equipped with Sutter filter wheels, prior mechanized stage and an environmental chamber (Solent) held at 37°C during measurements. The images were collected by Orca ERII camera cooled to −60°C, in the high precision (14 bit) mode using a ×20 PlanApochromat NA 0.8, PH2 objective. The filter sets are as follows: 430/25× (excitation) and 470/30 m (emission) for AmCyan, 565/55× (excitation) and 650/70 (emission) filters for DsRed-monomer, 430/25× (excitation) and 525/40 m (emission) for ZsGreen1. Data collection and processing were performed by the Metamorph 7.0 software.

FACS

The cells were prepared for the FACS analysis by trypsinizing each well with 0.5 ml 0.25% trypsin-EDTA, collecting the cell suspension and centrifuging at 4000 r.p.m. for 2 min. Trypsin was removed and the pellet was resuspended by short vortexing in 0.5 ml PBS buffer (Invitrogen). The cells were analyzed on a BD LSRII flow analyzer. AmCyan was measured with a 405-nm laser and a 450/50 emission filter, DsRed-monomer with a 488-nm laser and a 575/26 emission filter, and ZsGreen1 with a 488-nm laser and a 530/30 emission filter.

Cell culture

HEK293 Tet-On Advanced cell lines (Clontech, Cat # 630931) were used in all the experiments. The cells were grown at 37°C, 100% humidity, and 5% CO_2. The cells were initially transferred into CD-293 medium and a week later moved to the DMEM (Invitrogen, Cat # 11965-11810) supplemented with 0.1 mM of MEM non-essential amino acids (Invitrogen, Cat # 11140-050), 0.045 units/ml of Penicillin and 0.045 μg/ml Streptomycin (Penicillin–Streptomycin liquid; Invitrogen) and 10% FBS (Invitrogen). The adherent culture was maintained in this medium by trypsinizing with Trypsin-EDTA (0.25% Trypsin with EDTAx4Na; Invitrogen) and diluting in a fresh medium upon reaching 50–90% confluence.

Supplementary information

Supplementary information is available at the *Molecular Systems Biology* website (www.nature.com/msb).

Acknowledgements

The majority of experiments were performed at the FAS Center for Systems Biology at Harvard University. We thank the members of FAS CSB community for discussions. We thank Verena Jaeggin for assistance with cell sorting and Tobias Kockmann for assistance with qPCR. This research was supported by the Bauer Fellow Program, NIGMS Grant GM068763 and ETH start-up and core funding (YB), by UTD start-up funding (LB), and by Grants NIH 1R01GM086881, AFOSR FA9550-08, and NSF DMS-0614371 (ES).

Author contributions: YB and LB designed the research. LB performed most of the experiments and numerical simulations. LB, ZX, DG, AA, and YB made the DNA constructs. DG performed the initial measurements and simulations of the ptI1-FFL_{II} circuit. YB performed cell sorting and qPCR measurements. LB, YB, and ES analyzed the data. ES constructed the mathematical model. LB, YB, and ES wrote the paper. YB supervised the project.

Conflict of interest

The authors declare that they have no conflict of interest.

References

Acar M, Pando BF, Arnold FH, Elowitz MB, van Oudenaarden A (2010) A general mechanism for network-dosage compensation in gene circuits. *Science* **329:** 1656–1660

Balazsi G, Barabasi AL, Oltvai ZN (2005) Topological units of environmental signal processing in the transcriptional regulatory network of Escherichia coli. *Proc Natl Acad Sci USA* **102:** 7841–7846

Basu S, Mehreja R, Thiberge S, Chen MT, Weiss R (2004) Spatiotemporal control of gene expression with pulse-generating networks. *Proc Natl Acad Sci USA* **101:** 6355–6360

Becskei A, Serrano L (2000) Engineering stability in gene networks by autoregulation. *Nature* **405:** 590–593

Blake WJ, Kaern M, Cantor CR, Collins JJ (2003) Noise in eukaryotic gene expression. *Nature* **422:** 633–637

Boyer LA, Lee TI, Cole MF, Johnstone SE, Levine SS, Zucker JR, Guenther MG, Kumar RM, Murray HL, Jenner RG, Gifford DK, Melton DA, Jaenisch R, Young RA (2005) Core transcriptional regulatory circuitry in human embryonic stem cells. *Cell* **122:** 947–956

Cantone I, Marucci L, Iorio F, Ricci MA, Belcastro V, Bansal M, Santini S, di Bernardo M, di Bernardo D, Cosma MP (2009) A yeast synthetic network for *in vivo* assessment of reverse-engineering and modeling approaches. *Cell* **137:** 172–181

Cohen RN, van der Aa M, Macaraeg N, Lee AP, Szoka FC (2009) Quantification of plasmid DNA copies in the nucleus after lipoplex and polyplex transfection. *J Control Release* **135:** 166–174

Elowitz MB, Levine AJ, Siggia ED, Swain PS (2002) Stochastic gene expression in a single cell. *Science* **297:** 1183–1186

Entus R, Aufderheide B, Sauro H (2007) Design and implementation of three incoherent feed-forward motif based biological concentration sensors. *Syst Synth Biol* **1:** 119–128

Goentoro L, Shoval O, Kirschner MW, Alon U (2009) The incoherent feedforward loop can provide fold-change detection in gene regulation. *Mol Cell* **36:** 894–899

Holtz WJ, Keasling JD (2010) Engineering static and dynamic control of synthetic pathways. *Cell* **140:** 19–23

Isaacs FJ, Hasty J, Cantor CR, Collins JJ (2003) Prediction and measurement of an autoregulatory genetic module. *Proc Natl Acad Sci USA* **100:** 7714–7719

Kaplan S, Bren A, Dekel E, Alon U (2008) The incoherent feed-forward loop can generate non-monotonic input functions for genes. *Mol Syst Biol* **4:** 203

Keyomarsi K, Pardee AB (1993) Redundant cyclin overexpression and gene amplification in breast-cancer cells. *Proc Natl Acad Sci USA* **90:** 1112–1116

Kittisopikul M, Suel GM (2010) Biological role of noise encoded in a genetic network motif. *Proc Natl Acad Sci USA* **107:** 13300–13305

Lee T, Rinaldi N, Robert F, Odom D, Bar-Joseph Z, Gerber G, Hannett N, Harbison C, Thompson C, Simon I, Zeitlinger J, Jennings E, Murray H, Gordon B, Ren B, Wyrick J, Tagne J-B, Volkert T, Fraenkel E, Gifford D *et al* (2002) Transcriptional regulatory networks in Saccharomyces cerevisiae. *Science* **298:** 799–804

Leisner M, Bleris L, Lohmueller J, Xie Z, Benenson Y (2010) Rationally designed logic integration of regulatory signals in mammalian cells. *Nat Nanotechnol* **5:** 666–670

Lu TK, Khalil AS, Collins JJ (2009) Next-generation synthetic gene networks. *Nat Biotechnol* **27:** 1139–1150

Lucchesi JC, Kelly WG, Parming B (2005) Chromatin remodeling in dosage compensation. *Ann Rev Genet* **39:** 615–651

Ma WZ, Trusina A, El-Samad H, Lim WA, Tang C (2009) Defining network topologies that can achieve biochemical adaptation. *Cell* **138:** 760–773

Ma'ayan A, Jenkins SL, Neves S, Hasseldine A, Grace E, Dubin-Thalere B, Eungdamrong NJ, Weng GZ, Ram PT, Rice JJ, Kershenbaum A, Stolovitzky GA, Blitzer RD, Iyengar R (2005) Formation of regulatory patterns during signal propagation in a mammalian cellular network. *Science* **309:** 1078–1083

Mangan S, Alon U (2003) Structure and function of the feed-forward loop network motif. *Proc Natl Acad Sci USA* **100:** 11980–11985

Mangan S, Itzkovitz S, Zaslaver A, Alon U (2006) The incoherent feed-forward loop accelerates the response-time of the gal system of Escherichia coli. *J Mol Biol* **356:** 1073–1081

McCullagh E, Farlow J, Fuller C, Girard J, Lipinski-Kruszka J, Lu D, Noriega T, Rollins G, Spitzer R, Todhunter M, El-Samad H (2009) Not all quiet on the noise front. *Nat Chem Biol* **5:** 699–704

Milo R, Shen-Orr S, Itzkovitz S, Kashtan N, Chklovskii D, Alon U (2002) Network motifs: simple building blocks of complex networks. *Science* **298:** 824–827

Nakamoto M, Jin P, O'Donnell WT, Warren ST (2005) Physiological identification of human transcripts translationally regulated by a specific microRNA. *Hum Mol Genet* **14:** 3813–3821

Ozbudak EM, Thattai M, Kurtser I, Grossman AD, van Oudenaarden A (2002) Regulation of noise in the expression of a single gene. *Nat Genet* **31:** 69–73

Paulsson J (2004) Summing up the noise in gene networks. *Nature* **427:** 415–418

Pollard H, Remy JS, Loussouarn G, Demolombe S, Behr JP, Escande D (1998) Polyethylenimine but not cationic lipids promotes transgene delivery to the nucleus in mammalian cells. *J Biol Chem* **273:** 7507–7511

Raj A, Peskin CS, Tranchina D, Vargas DY, Tyagi S (2006) Stochastic mRNA synthesis in mammalian cells. *PLoS Biol* **4:** 1707–1719

Raser JM, O'Shea EK (2005) Noise in gene expression: origins, consequences, and control. *Science* **309:** 2010–2013

Rinaudo K, Bleris L, Maddamsetti R, Subramanian S, Weiss R, Benenson Y (2007) A universal RNAi-based logic evaluator that operates in mammalian cells. *Nat Biotechnol* **25:** 795–801

Russell RB, Aloy P (2008) Targeting and tinkering with interaction networks. *Nat Chem Biol* **4:** 666–673

Schwake G, Youssef S, Kuhr JT, Gude S, David MP, Mendoza E, Frey E, Radler JO (2010) Predictive modeling of non-viral gene transfer. *Biotechnol Bioeng* **105:** 805–813

Shen-Orr SS, Milo R, Mangan S, Alon U (2002) Network motifs in the transcriptional regulation network of Escherichia coli. *Nat Genet* **31:** 64–68

Shoval O, Goentoro L, Hart Y, Mayo A, Sontag E, Alon U (2010) Fold change detection and scalar symmetry of sensory input fields. *Proc Natl Acad Sci* **107:** 15995–16000

Sontag ED (2010) Remarks on feedforward circuits, adaptation, and pulse memory. *IET Syst Biol* **4:** 39–51

Stenberg P, Lundberg LE, Johansson AM, Ryden P, Svensson MJ, Larsson J (2009) Buffering of segmental and chromosomal aneuploidies in Drosophila melanogaster. *PLoS Genet* **5:** 10

Tsang J, Zhu J, van Oudenaarden A (2007) MicroRNA-mediated feedback and feedforward loops are recurrent network motifs in mammals. *Mol Cell* **26:** 753–767

Tseng WC, Haselton FR, Giorgio TD (1997) Transfection by cationic liposomes using simultaneous single cell measurements of plasmid delivery and transgene expression. *J Biol Chem* **272:** 25641–25647

Tyson JJ, Chen KC, Novak B (2003) Sniffers, buzzers, toggles and blinkers: dynamics of regulatory and signaling pathways in the cell. *Curr Opin Cell Biol* **15:** 221–231

Veitia RA, Bottani S, Birchler JA (2008) Cellular reactions to gene dosage imbalance: genomic, transcriptomic and proteomic effects. *Trends Genet* **24:** 390–397

Supplemental Information

Synthetic Incoherent Feedforward Circuits Show Adaptation to the Amount of their Genetic Template.

Leonidas Bleris, Zhen Xie, David Glass, Asa Adadey, Eduardo Sontag, Yaakov Benenson

Supplemental Figures

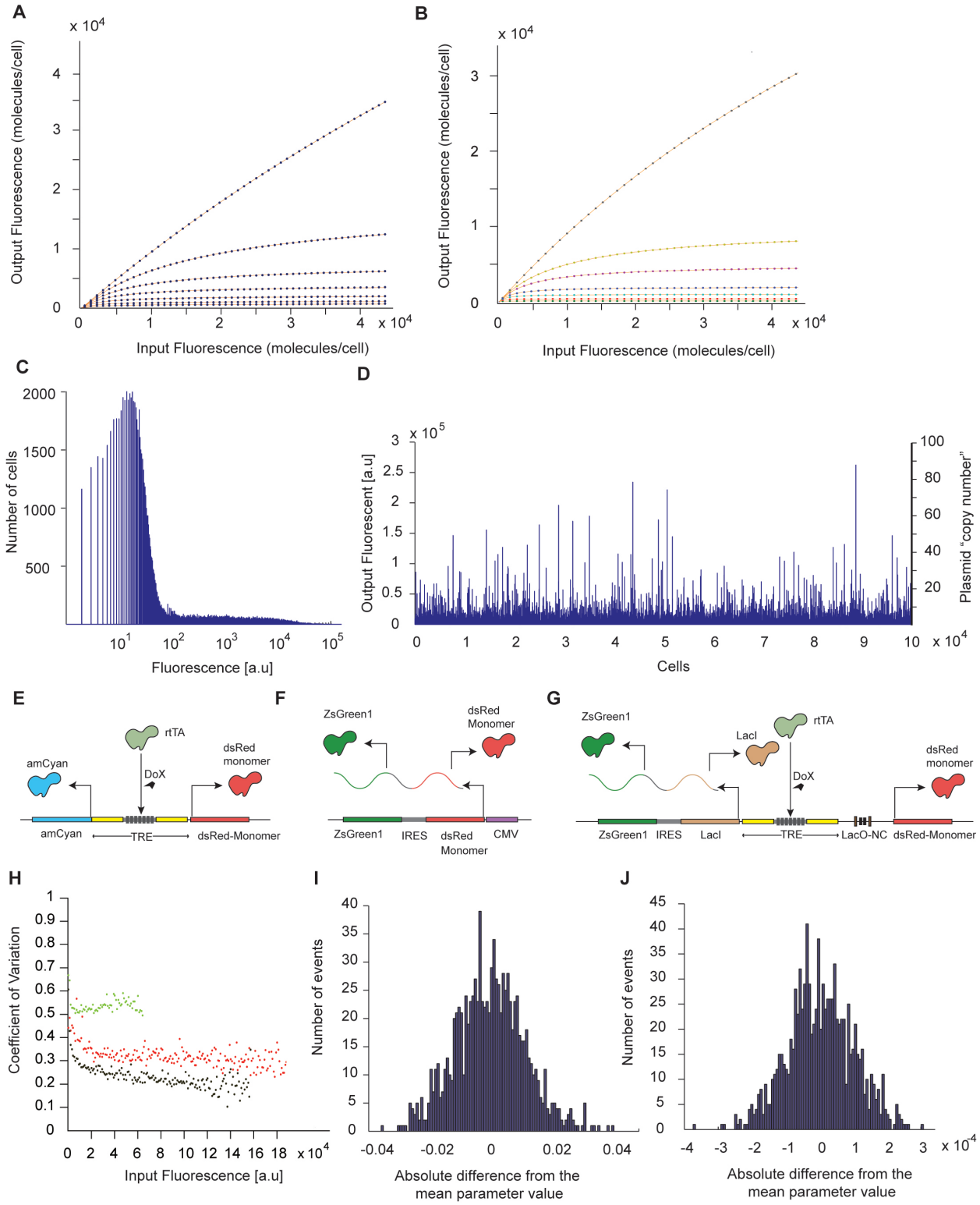

Supplementary Figure 1. Simulation details. (**A**) Parametric simulations of the transcriptional I1-

FFL input-output behavior (dots) for a range of binding constants (Figure 2B) and the fitting to the rational function $\sigma(x)=c(x+a)/(x+b)$ (orange curves). (**B**) Parametric simulations of the post-transcriptional I1-FFL_I input-output behavior (dots) for a range of RNAi degradation rates (Figure 2F) and the fitting to the rational function $\sigma(x)=c(x+a)/(x+b)$ (orange curves). (**C**) Histogram of ZsGreen fluorescent protein levels in transiently-transfected cells measured using flow cytometry. In this experiment, 400 ng of plasmid carrying constitutively-expressed, CMV-driven LacI-IRES-zsGreen1 construct was transfected into HEK293 TET-On cells and measured after 48 hours. (**D**) "Time series" of the fluorescence level in single cells, picked from the distrbution in panel C and used for noisy simulations. The first Y axis shows fluorescence in instrument units, the second axis shows this intensity converted to a "copy-number" using an arbitrary scaling factor. (**E-H**) Constructs used to characterize the intrinsic noise of the pTRE promoter and the IRES element. All experiments were performed in the presence of 1000 ng/ml Dox. (**E**) A construct pTRE-Tight-BI-amCyan-DsRed with a pTRE bidirectional promoter driving the expression of amCyan and DsRed. (**F**) A construct DsRed-pIRES2-zsGreen1 constituvely driving the expression of a single IRES-connected ZsGreen1/DsRed-encoding transcript. (**G**) Transcriptional I1-FFL construct with a fully mutated LacO sequence, pTRE-Tight-BI-LacI-IRES-ZsGreen1-$LacO_{NegCtrl}$-DsRed. (**H**) Measured coefficient of variation of one fluorescent output level for a given level of another protein designated as input. pTRE-Tight-BI-LacI-IRES-ZsGreen1-$LacO_{NegCtrl}$-DsRed is shown in green (input: ZsGreen, output: DsRed), DsRed-pIRES2-zsGreen1 in shown in red (input: ZsGreen, output: DsRed), and pTRE-Tight-BI-amCyan-DsRed is shown in black (input: DsRed, output: AmCyan). (**I, J**) Normal distributions used for incorporating noise in "noisy" simulations. (**I**) Normal distribution characterizing pTRE promoter, rescaled to have the mean value of zero and standard deviation equaling to 25% of

0.0467 sec^{-1}, the rate of expression from pTRE proimoter used in simulations. (**J**) A normal distribution characterizing the IRES element, rescaled to have the mean value of zero mean and standard deviation equaling to 30% of 0.00033 sec^{-1}, the basic translation rate used in simulations.

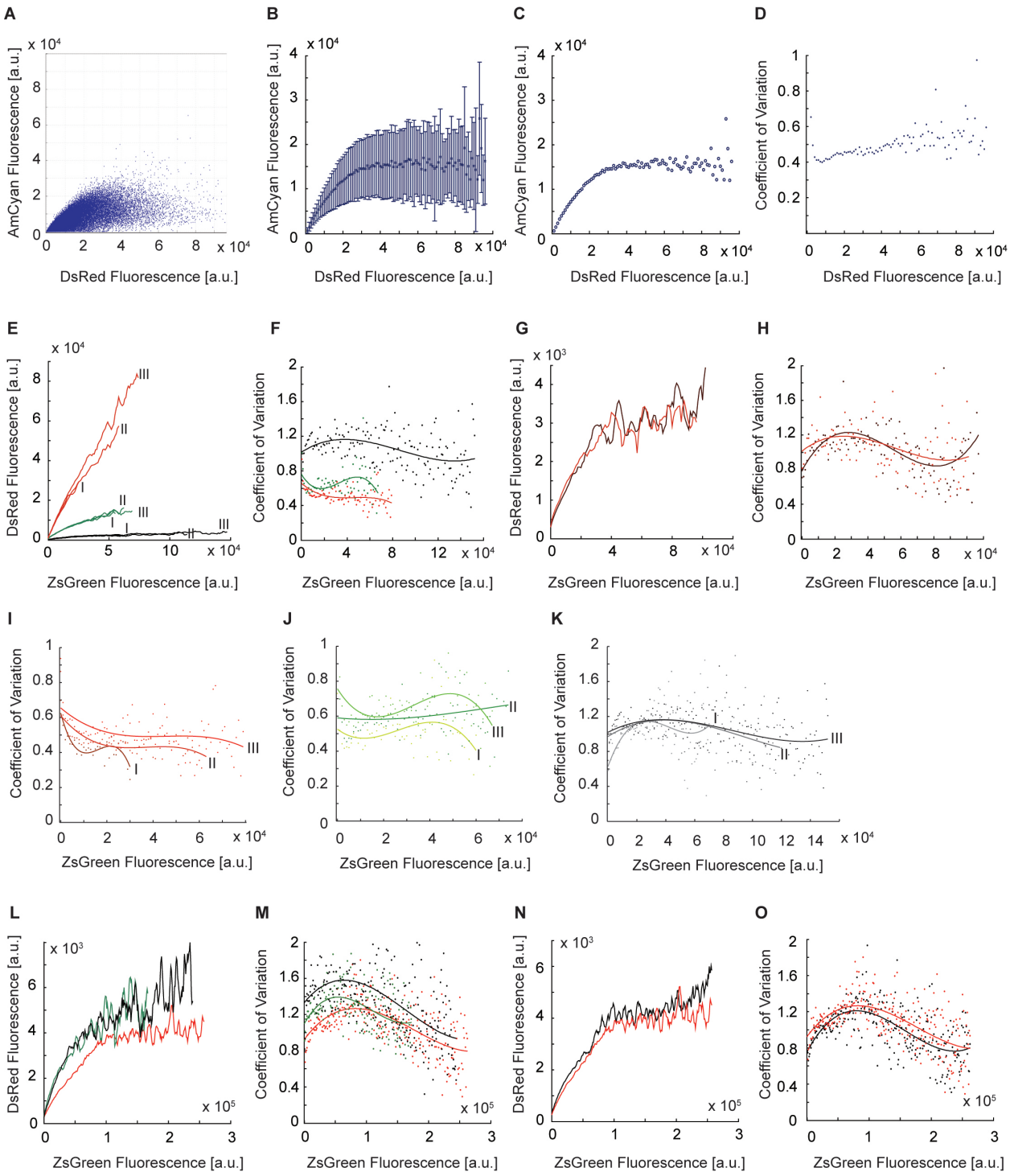

Supplementary Figure 2. Experimental implemenation of the circuits. (**A**) An example of raw flow cytometry data measured with post-transcriptional I1-FFL circuit. (**B-D**) An illustration of

the binning processing using data from panel A. (**B**) The mean value and the standard deviation of the output values in each bin of 1000 fluorescence units. (**C**) The plot of mean values for each bin. (**D**) The plot of coefficient of variation values for each bin. (**E-H**) Titration of plasmid and Dox concentration for the transcriptional I1-FFL. (**E**) I, II and III indicate 200, 400 and 800 ng of the circuit-encoding plasmid, respectively. Red, green and black color indicate LacO mutant 4, LacO mutant 1 and wild-type LacO, respectively. These experiments were performed using Lipofectamine PLUS transfection reagents with 1000 ng/ml Dox. (**F**) Coefficients of variation measured with different LacO variants with red, green and black color corresponding to 800 ng of LacO mutant 4, LacO mutant 1 and wild-type LacO, respectively. (**G**) Input-output response with different Dox concentrations. 1000 ng of the wild type LacO tI1-FFL circuit plasmid were transfected in the presence of 1000 ng/mL (red) or 4000 ng/mL (black) Dox. (**H**) Coefficients of variation measured for the experiments in panel G, using the same color coding. (**I-K**). Coefficients of variation measured in all the experiments shown in panel E. Latin numerals and color-coding are the same. (**L-O**) Effects of different transfection reagents and wait times prior to measurements on the transcriptional I1-FFL. (**L**) 1000 ng of the wild type I1-FFL using Lipofectamine 2000 (black), 500 ng of the wild type I1-FFL using Lipofectamine-PLUS (green), and 500 ng of the wild type I1-FFL using LipoLTX (red). All the experiments are performed in the presence of 1000 ng/ml Dox. (**M**) Coefficient of variation for the experiments detailed in panel L using the same color-coding. (**N**) 500 ng of the wild type I1-FFL transfected using LipoLTX measured 48h post-tranfection (red) and 72h post-transfection (black). (**O**) Coefficient of variation for the experiments detailed in panel C, same color-coding.

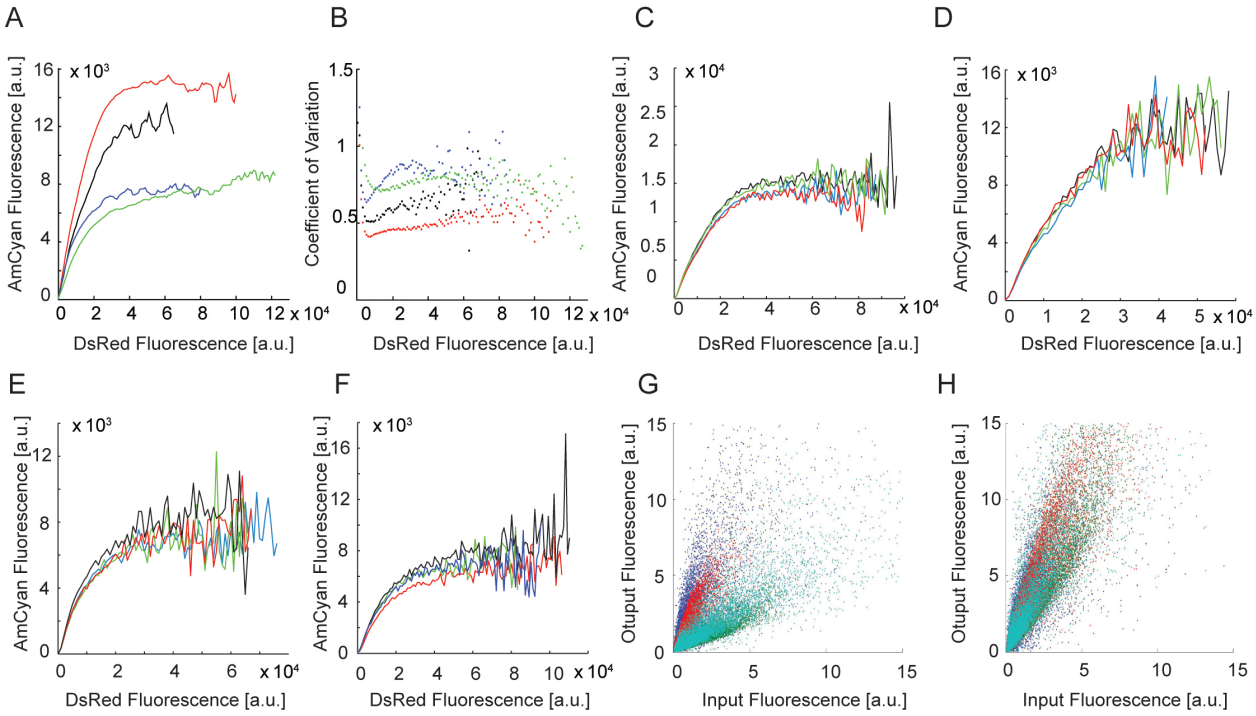

Supplementary Figure 3. Calibration of experimental conditions for the post-transcriptional I1-FFL, version I. (**A, B**) Titration of concentrations and comparison of transfection reagents. (**A**) 250 ng of the ptI1-FFL-ver1 using Lipofectamine PLUS (blue), 500ng of the ptI1-FFL-ver1 using Lipofectamine PLUS (black), 500 ng of the ptI1-FFL-ver1 using Lipofectamine 2000 (green), and 500 ng of the ptI1-FFL-ver1 using LipoLTX (red). All the experiments are performed in the presence of 1000 ng/ml Dox. (**B**) Coefficient of variation measured in the experiments detailed in panel a using the same color-coding. (**C-F**) Reproducibility of the input-output behavior observed with different combinations of plasmid amounts and transfection reagents used in panel A. (**C**) Four repeats transfecting 500 ng of the ptI1-FFL-ver1 using LipoLTX (same conditions as the red curve in panel A). (**D**) Four repeats transfecting 500 ng of the ptI1-FFL-ver1 using Lipofectamine PLUS (same conditions as the black curve in panel A). (**E**) Four repeats transfecting 250 ng of the ptI1-FFL-ver1 using Lipofectamine PLUS (same

conditions as the blue curve in panel A). (**F**) Four repeats transfecting 500 ng of the ptI1-FFL-ver1 using Lipofectamine 2000 (same conditions as the green curve in panel A). (**G, H**) Illustration of the normalization procedure used to compare different circuits with different input and output fluorophores. (**G**) Raw scatter plots of the negative control of the four different constructs (blue: tI1-FFL, green: I1-FFL-ver1, red: I1-FFL-ver2, cyan: tAM). (**H**) Normalized scatter plots. 20,000 cells are shown for illustration.

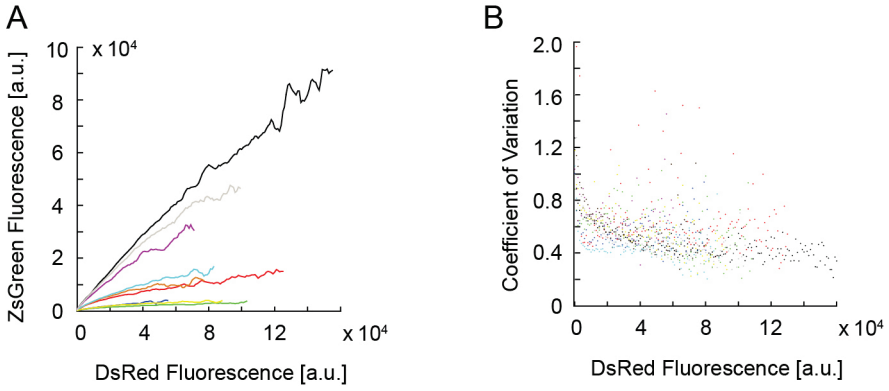

Supplementary Figure 4. Effect of transfection reagents for the transcriptional negative autoregulator. All experiments are performed using 500 ng of the plasmid in the presence of 1000 ng/ml Dox. (**A**) LipoLTX reagent: 2xLaO trAM (green), 1xLaO trAM (red), and 1xLacO trAM with 1M IPTG (black). Lipofectamine Plus: 2xLaO trAM (blue), 1xLaO trAM (orange), and 1xLacO trAM with 1M IPTG (purple). Lipofectamine 2000: 2xLaO trAM (yellow), 1xLaO trAM (cyan), and 1xLacO trAM with 1M IPTG (gray). (**B**) Coefficient of variation for all the experiments in panel A, using the same color-coding.

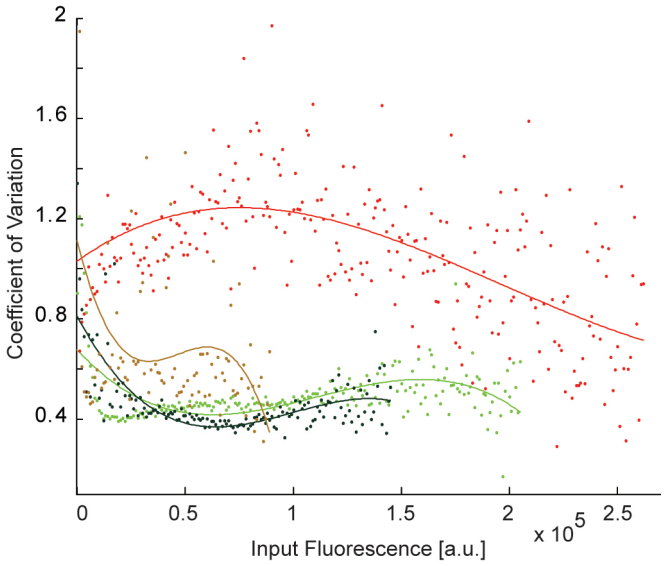

Supplementary Figure 5. Coefficient of variation for the motifs. Coefficient of variation in individual bins for each of the circuits; red: transcriptional incoherent feedforward loop; brown: transcriptional autoregulation; green: post-transcriptional incoherent feedforward motif version I; black: post-transcriptional incoherent feedforward motif version II.

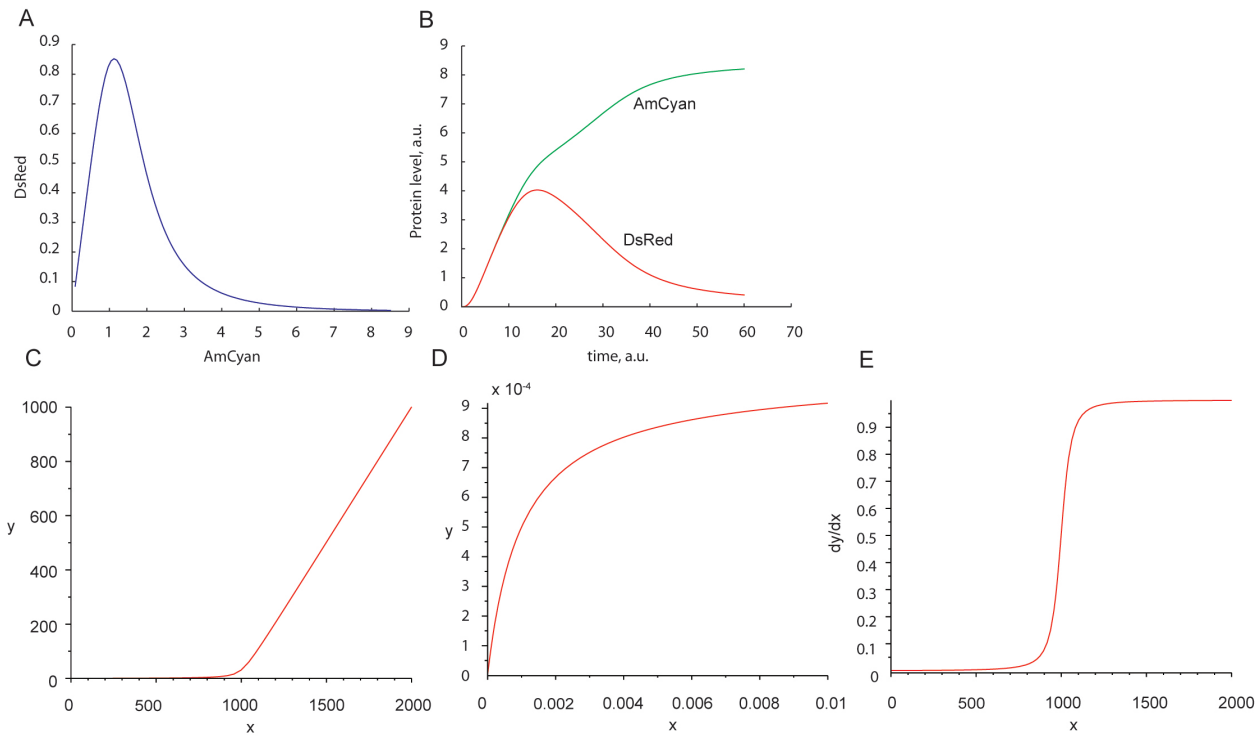

Supplementary Figure 6. Analytical simulations of the circuits. (**A**) Steady state levels of output (DsRed) vs input (AmCyan) in a special case of biphasic behavior. (**B**) Dynamic development of the input and output levels in biphasic case. (**C**) Plot of output (y) vs input (x) for post-transcriptional circuit showing almost constant behavior for $x < 500$ and linear behavior ($y = x +$ constant) for large x, as predicted from approximate analysis. (**D**) Zooming in the plot in panel C to show initial saturation behavior at $y = 0{:}001$. (**E**) Plot of derivative dy/dx, showing both an almost zero initial slope (adaptation) and an eventual nonzero constant slope (linear regime).

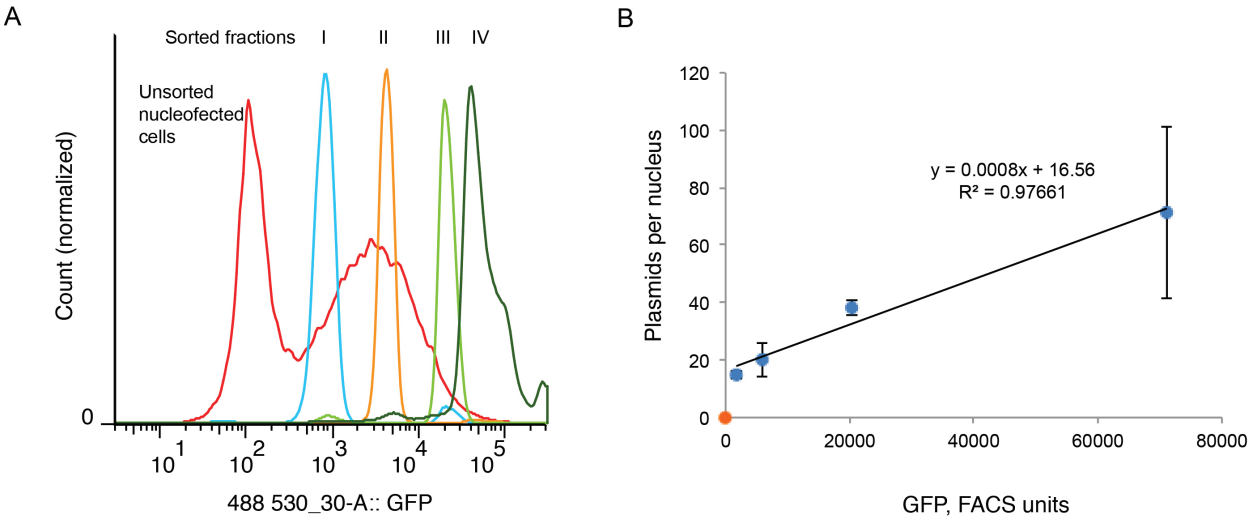

Supplementary Figure 7. Quantification of the relation between fluorescence and plasmid copy number. (**A**) Flow cytometry analysis of four FACS-sorted cell fractions overlaid on the flow cytometry distribution of the original unsorted population. Note that each fraction is normalized to the highest value in its own group. (B) Quantitative results of qPCR measurements, normalized to an internal control gene ACTB and based on the assumption that most 293 cells are triploid (based on ATCC record).

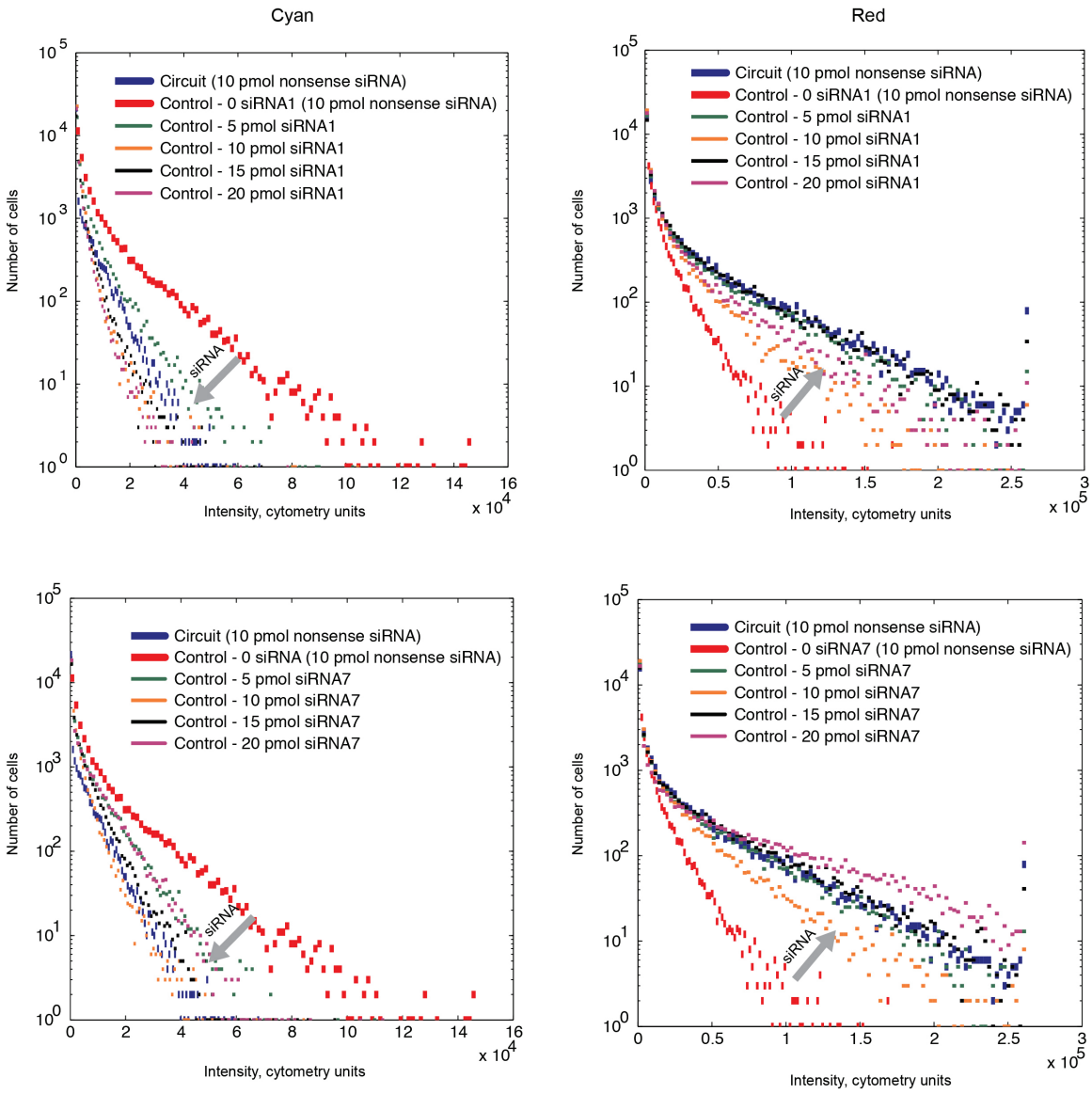

Supplementary Fig. 8. Effect of RNAi-induced knockdown of the output on the distribution of the input in ptI1-FFL$_I$. Histograms of AmCyan and DsRed obtained in flow cytometry experiments are shown as indicated. The top row shows data obtained with anti-AmCyan siRNA-1 and the bottom row shows data measured with anti-AmCyan siRNA-7.

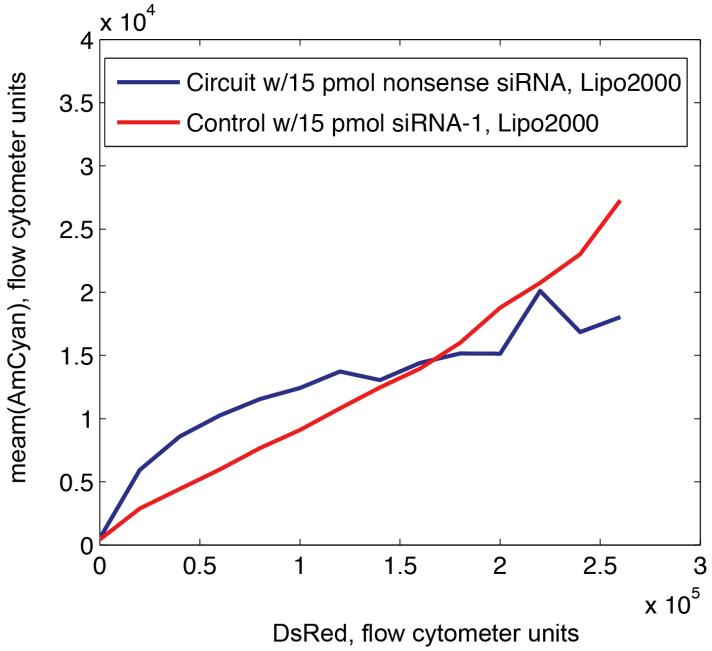

Supplementary Figure 9. siRNA-induced knock-down of AmCyan in a control circuit does not lead to adaptive input-output relationship. A representative comparison is shown, in which the distributions of both AmCyan and DsRed are similar between the siRNA-targeted control and the circuit. Despite similarity of the cumulative distributions, the siRNA-targeted control does not exhibit adaptive behavior.

Supplemental Tables

Supplementary Table 1. Estimated parameter values of the fit of the simulated tI1-FFL and pI1-FFL_I to the rational function **$y=\sigma(x)=c(x+a)/(x+b)$**.

Motif	LacI K_{on}	a	b (EC_{50})	c	R^2
tI1-FFL	3.3300e-7	-0.058667	1.7087e5	1.7092e5	1.00
tI1-FFL	3.3300e-6	1.6532	17583	17401	1.00
tI1-FFL	8.3250e-6	3.2408	7720.6	7246.6	1.00
tI1-FFL	1.6650e-5	3.8466	4504.6	3813.7	1.00
tI1-FFL	3.3300e-5	4.6685	3013.5	2062.6	1.00
tI1-FFL	6.6600e-5	7.4365	2601.9	1171.1	0.99
tI1-FFL	1.3320e-4	19.799	3488.3	731.82	0.99
Motif	miRNA K_{on}	a	b (EC_{50})	c	R^2
pI1-FFL_I	1.84e-9	0.016157	98518	98614	1.00
pI1-FFL_I	1.84e-8	0.0014108	9849.4	9859.4	1.00
pI1-FFL_I	3.7e-8	-3.1354e-4	4924.7	4929.8	1.00
pI1-FFL_I	9.2e-8	1.5222e-4	1969.9	1971.8	1.00
pI1-FFL_I	1.84e-7	-2.364e-5	984.84	985.93	1.00
pI1-FFL_I	4.6e-7	3.5341e-5	393.99	394.37	1.00
pI1-FFL_I	1.84e-6	2.3436e-6	98.462	98.591	1.00

Supplementary Table 2. Estimated parameter values, their confidence intervals and the coefficient of determination of the fit to the rational function **$y=\sigma(x)=c(x+a)/(x+b)$** calculated for the input-output dependency of the different circuits.

Motif	Variant	a	Conf. Int.	b (EC_{50})	Conf. Int.	C	Conf. Int.	R^2
tI1-FFL	Wild Type	-988.27	2000.8	53959	8521.7	5475.9	188.2	0.93
tI1-FFL	Mutant 1	6699.5	2937	197930	37162	72973	6955	0.97
tI1-FFL	Mutant 2	10148	3376	276860	58344	168460	20428	0.97
tI1-FFL	Mutant 3	5887.2	2136	274860	38380	219650	17567	0.99
tI1-FFL	Mutant 4	3573.7	873	205640	29838	335980	33218	1.00
tI1-FFL	Neg. Con.	2042.6	732	145750	30550	388250	57629	1.00
$pI1\text{-}FFL_I$	1xF3	-3192.4	849	27955	3423	54677	1236.3	0.96
$pI1\text{-}FFL_I$	Neg. Con.	796.01	131.6	113030	4461.4	349250	9269.1	1.00
$pI1\text{-}FFL_{II}$	1xF3	-2939.6	1215	82128	11617	95712	5562	0.98
$pI1\text{-}FFL_{II}$	Neg. Con.	-1018.2	260.3	6.29e15	1.0179e24	1.18e16	1.9215e24	1.00
tAM	2xLacO	6209.9	2683	71764	26481	11685	2078	0.96
tAM	1xLacO	5511.9	1732	128100	31346	66880	9639	0.99
tAM	Neg. Con.	368.89	530	233110	48744	541510	89683	1.00

Supplementary Table 3. Estimated parameter values, their confidence intervals and the coefficient of determination of the fit to the function $\boldsymbol{\pi_1(x)}= - a+(a^2+bx)^{1/2}$ calculated for the input-output dependency of the different circuits.

Motif	Variant	a	Conf. Int.	b	Conf. Int.	c	Conf. Int.	R^2
tI1-FFL	Wild Type	818.1	599.82	2.62e6	1.29e7	0.3168	0.0551	0.87*
tI1-FFL	Mutant 1	950.64	1514.9	446.07	665.3	0.5786	0.0457	0.98*
tI1-FFL	Mutant 2	-227.64	25227	287.54	376.9	0.6283	0.0448	0.98*
tI1-FFL	Mutant 3	1869.1	2476.9	290.6	280.1	0.6432	0.0337	0.99*
tI1-FFL	Mutant 4	-927.7719	1500	76.0176	38	0.7353	0.0228	1.00*
tI1-FFL	Neg. Con.	-949.13	2010.4	80.524	50.7	0.7585	0.0304	1.00*
$pI1\text{-}FFL_I$	1xF3	-7911.5	7026.5	8.97e9	6.41e10	0.3126	0.0607	0.85*
$pI1\text{-}FFL_I$	Neg. Con.	-1299.4	1579.6	106.7	51.2625	0.7498	0.0226	1.00*
$pI1\text{-}FFL_{II}$	1xF3	-9740.4	4192.2	49555	130700	0.4930	0.0554	0.96*
$pI1\text{-}FFL_{II}$	Neg. Con.	805.429	359.99	0.7892	0.0751	1.08	0.0094	1.00*
tAM	2xLacO	451	381.7211	65.6953	138.4487	0.5664	0.0749	0.97*
tAM	1xLacO	945.6381	909.4237	80.4426	92.2213	0.6502	0.0460	0.99*
tAM	Neg. Con.	-967.2	1929.7	14.9831	8.4	0.8490	0.341	1.00*
*fitting algorithm reached maximum number of iterations								

Supplementary Table 4. Estimated parameter values, their confidence intervals and the coefficient of determination of the fit to the function $\boldsymbol{\pi_2(x)}$ =a+(bx)^c calculated for the input-output dependency of the different circuits.

Motif	Variant	a	Conf. Int.	b	Conf. Int.	R^2
tI1-FFL	Wild Type	323.05	117.92	82.52	6.8296	0.85
tI1-FFL	Mutant 1	5606.6	1294.7	9602.1	651.3431	0.98
tI1-FFL	Mutant 2	13052	2680.3	37254	2533	0.98
tI1-FFL	Mutant 3	27637	3654	72419	4215.3	0.99
tI1-FFL	Mutant 4	49847	5375	2.4166e5	14514	1.00
tI1-FFL	Neg. Con.	63773	9289	4.7344e5	41534	1.00
pI1-FFL$_I$	1xF3	-3903.5	1519.4	11815	1214.9	0.82
pI1-FFL$_I$	Neg. Con.	77424	4692	5.7462e5	22339	1.00
pI1-FFL$_{II}$	1xF3	14299	4239.3	39971	4629.8	0.96
pI1-FFL$_{II}$	Neg. Con.	5.5622e12	1.5904e13	2.0471e13	5.854e13	1.00
tAM	2xLacO	-120.51	148.91	546.15	39.59	0.97
tAM	1xLacO	4102.6	1047.5	12112	894.5	0.97
tAM	Neg. Con.	175470	27590	861240	108980	1.00

Supplementary Table 5. Estimated parameter values, their confidence intervals and the coefficient of determination of the fit to the linear function $\lambda(x)=a+bx$ calculated for the experimentally-measured input-output dependency of the different circuits.

Motif	Variant	a	Conf. Int.	b	Conf. Int.	R^2
tI1-FFL	Wild	0.01303	0.001	1746.2	148.5616	0.72

	Type					
tI1-FFL	Mutant 1	0.17378	0.0058	7005.6	642.8080	0.95
tI1-FFL	Mutant 2	0.33418	0.0097	12974	1103.4	0.96
tI1-FFL	Mutant 3	0.43472	0.0109	14459	1287.4	0.97
tI1-FFL	Mutant 4	1.0871	0.0250	12927	1357.9	0.99
tI1-FFL	Neg. Con.	1.8497	0.0513	12148	1753.3	0.99
pI1-FFL_I	1xF3	0.16801	0.0172	19924	1989	0.65
pI1-FFL_I	Neg. Con.	2.0203	0.0587	10864	1905.8	0.99
pI1-FFL_{II}	1xF3	0.40273	0.0218	9584.5	1768.5	0.91
pI1-FFL_{II}	Neg. Con.	1.8878	0.0144	-1923.5	499.2941	1.00
tAM	2xLacO	0.072899	0.0044	1682.4	176.5924	0.94
tAM	1xLacO	0.2947	0.011	5260.9	536.4035	0.97
tAM	Neg. Con.	1.8222	0.0361	5545.5	1297.1	1.00

Supplemental Experimental Procedures

1. Simulations

1.1. Deterministic simulations

Simbiology diagram used to simulate a transcriptional incoherent motif is shown below:

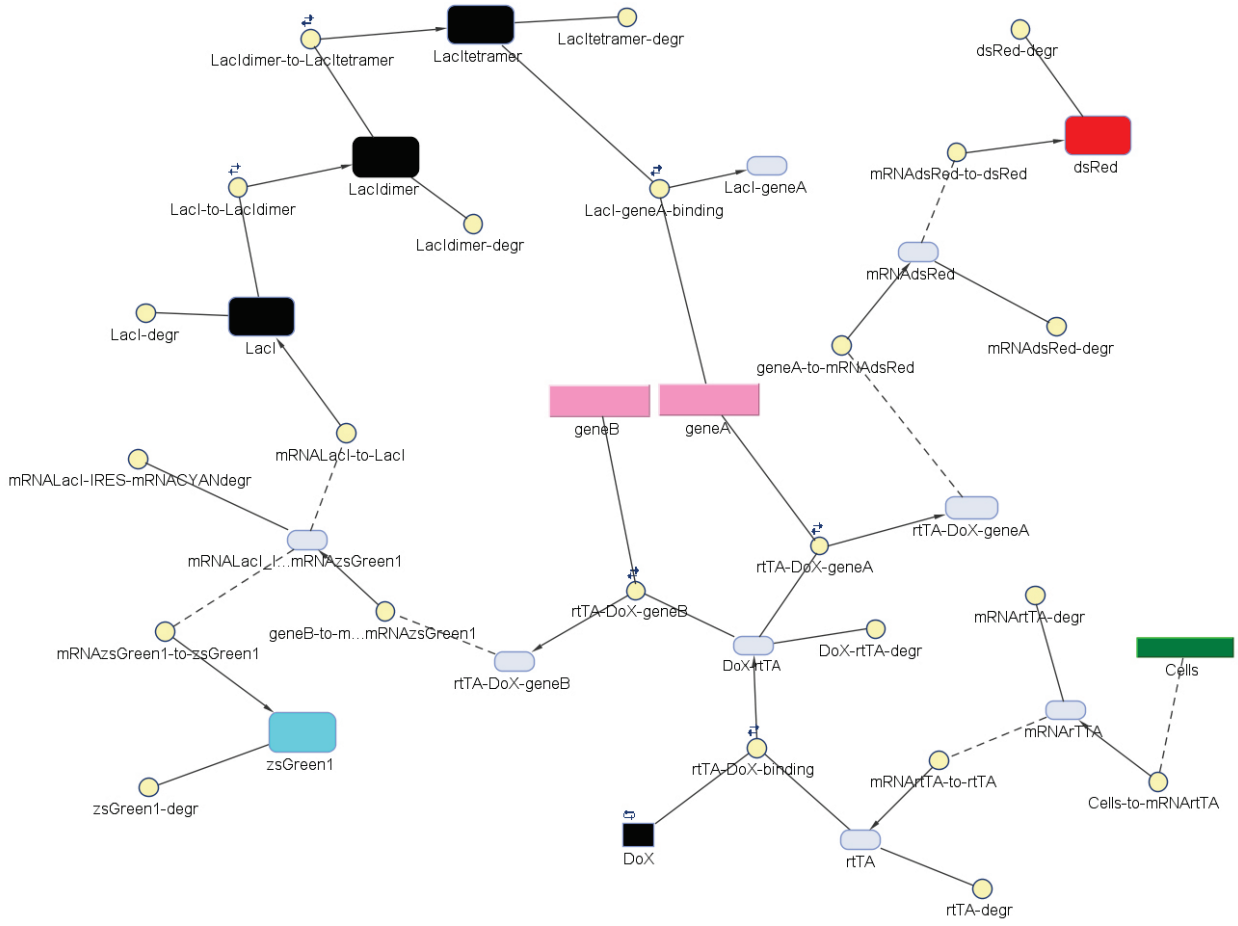

This diagram corresponds to the following reaction array:

[rtTA-DoX-geneA] -> mRNAdsRed + [rtTA-DoX-geneA]
mRNAdsRed -> dsRed + mRNAdsRed
mRNAdsRed -> null
dsRed -> null
geneA + LacItetramer <-> [LacI-geneA]

zsGreen1 -> null
mRNALacI_IRES_mRNAzsGreen1 -> zsGreen1 + mRNALacI_IRES_mRNAzsGreen1
[rtTA-DoX-geneB] -> [rtTA-DoX-geneB] + mRNALacI_IRES_mRNAzsGreen1
[DoX-rtTA] -> null
rtTA -> null
[DoX-rtTA] + geneB <-> [rtTA-DoX-geneB]
DoX + rtTA <-> [DoX-rtTA]
[DoX-rtTA] + geneA <-> [rtTA-DoX-geneA]
LacI -> null
LacItetramer -> null
mRNALacI_IRES_mRNAzsGreen1 -> LacI + mRNALacI_IRES_mRNAzsGreen1
2 LacI <-> LacIdimer
2 LacIdimer <-> LacItetramer
LacIdimer -> null
mRNALacI_IRES_mRNAzsGreen1 -> null
Cells -> Cells + mRNArTTA
mRNArTTA -> null
mRNArTTA -> mRNArTTA + rtTA

The parameters used in simulations are as follows:

	Value	Units	Reference
k-geneA-to-mRNAdsRed	0.0467	1/second	(Tigges et al, 2009)
k-mRNAdsRed-to-dsRed	0.00033333	1/second	(Tigges et al, 2009;Tigges et al, 2010)
k-mRNAdsRed-degr	0.00034	1/second	(Tigges et al, 2009)
k-dsRed-degr	0.000096667	1/second	(Tigges et al, 2009)
kON-LacI-geneA-binding	0.0000333	1/(molecule*second)	(Ozbudak et

			al, 2004)
kOFF-LacI-geneA-binding	0.001	1/second	(Ozbudak et al, 2004)
k-zsGreen1-degr	0.000096667	1/second	(Tigges et al, 2009)
k-mRNAzsGreen1-to-zsGreen1	0.00033333	1/second	(Tigges et al, 2009;Tigges et al, 2010)
k-geneB-to-mRNALacI_IRES_mRNACyan	0.0467	1/second	(Tigges et al, 2009)
k-DoX-rtTA-degr	0.000096667	1/second	(Tigges et al, 2009)
k-rtTA-degr	0.000096667	1/second	(Tigges et al, 2009)
kON-rtTA-DoX-geneB-binding	0.000000028	1/(molecule*second)	(Tigges et al, 2009)
kOFF-rtTA-DoX-geneB-binding	0.00001	1/second	(Tigges et al, 2009)
kON-rtTA-DoX-binding	0.00001	1/(molecule*second)	(To & Maheshri, 2010)
kOFF-rtTA-DoX-binding	0.00000002	1/second	(To & Maheshri, 2010)
kOFF-rtTA-DoX-geneA-binding	0.00001	1/second	(Tigges et al, 2009)
kON-rtTA-DoX-geneA-binding	0.000000028	1/(molecule*second)	(Tigges et al, 2009)
k-LacI-degr	0.000096667	1/second	(Tigges et al, 2009)
k-LacItetramer-degr	0.000096667	1/second	(Tigges et al,

			2009)
k-mRNALacI-to-LacI1	0.00033333	1/second	(Tigges et al, 2009;Tigges et al, 2010)
kON-LacI-to-LacIdimer	0.0004637	1/(molecule*second)	(Hsieh & Brenowitz, 1997)
kOFF-LacI-to-LacIdimer	0.00000001	1/second	(Hsieh & Brenowitz, 1997)
kON-LacIdimer-to-LacItetramer	0.000602	1/(molecule*second)	(Hsieh & Brenowitz, 1997)
kOFF-LacIdimer-to-LacItetramer	0.000001	1/second	(Hsieh & Brenowitz, 1997)
k-LacIdimer-degr	0.000096667	1/second	(Tigges et al, 2009)
k-mRNALacI-IRES-mRNAZsGreen1-degr	0.00034	1/second	(Tigges et al, 2009)
k-Cells-to-mRNArtTA	0.0467	1/second	(Tigges et al, 2009)
k-mRNrtTA-degr	0.00034	1/second	(Tigges et al, 2009)
k-mRNArtTA-to-rtTA	0.00033333	1/second	(Tigges et al, 2009;Tigges et al, 2010)

Simbiology diagram used to simulate a post-transcriptional incoherent motif is shown below:

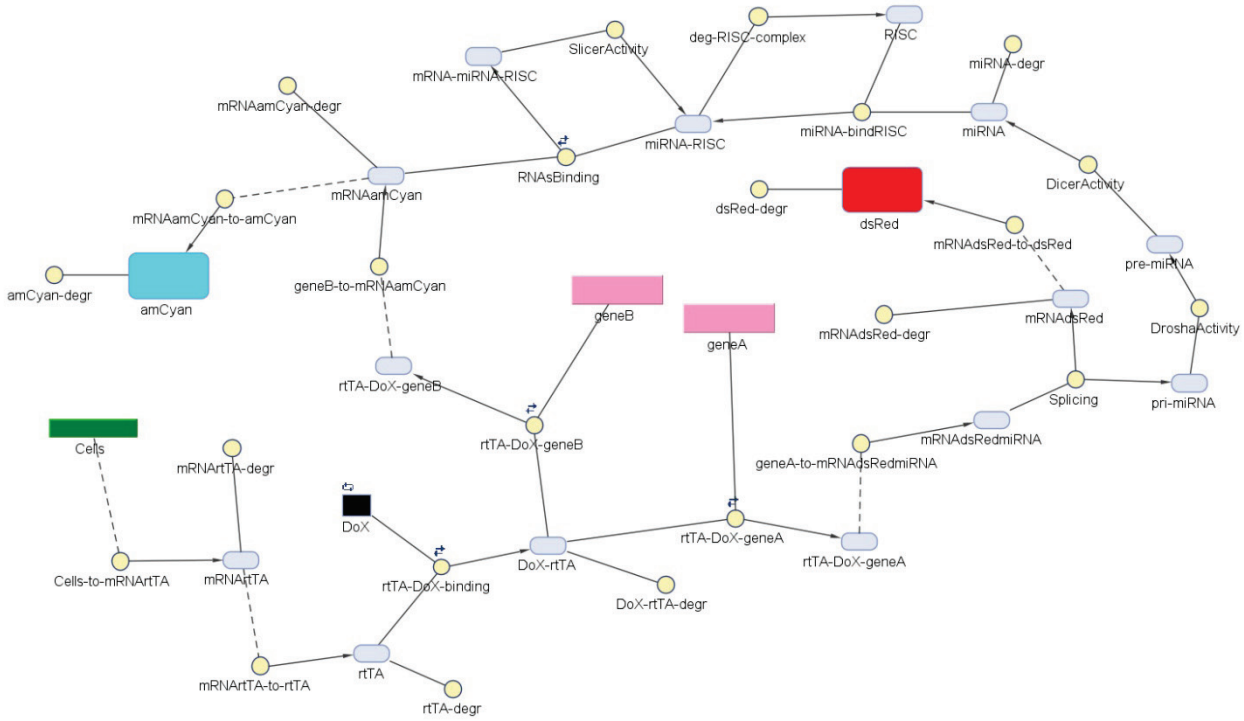

This diagram coresponds to the following reaction array:

[rtTA-DoX-geneA] -> mRNAdsRedmiRNA + [rtTA-DoX-geneA]
mRNAdsRed -> mRNAdsRed + dsRed
mRNAdsRedmiRNA -> [pri-miRNA] + mRNAdsRed
[pri-miRNA] -> [pre-miRNA]
[pre-miRNA] -> miRNA
miRNA_RISC + mRNAamCyan <-> mRNA_miRNA_RISC
mRNA_miRNA_RISC -> miRNA_RISC
dsRed -> null
mRNAdsRed -> null
miRNA -> null
miRNA_RISC -> RISC
miRNA + RISC -> miRNA_RISC
mRNArTTA -> mRNArTTA + rtTA
mRNArTTA -> null

Cells -> Cells + mRNArTTA
mRNAamCyan -> null
[DoX-rtTA] + geneA <-> [rtTA-DoX-geneA]
DoX + rtTA <-> [DoX-rtTA]
[DoX-rtTA] + geneB <-> [rtTA-DoX-geneB]
rtTA -> null
[DoX-rtTA] -> null
[rtTA-DoX-geneB] -> [rtTA-DoX-geneB] + mRNAamCyan
mRNAamCyan -> amCyan + mRNAamCyan
amCyan -> null

The parameters used in simulations are as follows:

	Value	Units	Reference
k_geneA-to-mRNAdsRedmiRNA	0.0467	1/second	(Tigges et al, 2009)
k_ mRNAdsRed-to-dsRed	0.000333	1/second	(Tigges et al, 2009;Tigges et al, 2010)
k_Splicing	0.002	1/second	Estimate
k_Drosha	0.01	1/second	Estimate
k_Dicer	0.001	1/second	(Tigges et al, 2010)
k_RISC_formation	0.00000184	1/(molecule*second)	(Tigges et al, 2010)
k_RISC_de-formation	0.01	1/second	(Tigges et al, 2010)
k_Slicer	0.007	1/second	(Tigges et al, 2010)
k_dsRed-degr	0.000096667	1/second	(Tigges et al, 2009)

k_mRNAdsRed-degr	0.000288	1/second	(Tigges et al, 2009)
k_miRNA-degr	0.000288	1/second	(Tigges et al, 2009)
k_RISKcomlpex-degr	0.0000216	1/second	(Tigges et al, 2010)
k_miRNAbindRISK	0.00001	1/(molecule*second)	(Tigges et al, 2010)
k-mRNArtTA-to-rtTA	0.00033333	1/second	(Tigges et al, 2009;Tigges et al, 2010)
k-mRNrtTA-degr	0.000288	1/second	(Tigges et al, 2009)
k-Cells-to-mRNArtTA	0.0467	1/second	(Tigges et al, 2009)
k-mRNAamCyan-degr	0.000288	1/second	(Tigges et al, 2009)
kOFF-rtTA-DoX-geneA-binding	0.00001	1/second	(Tigges et al, 2009)
kON-rtTA-DoX-geneA-binding	0.000000028	1/(molecule*second)	(Tigges et al, 2009)
kON-rtTA-DoX-binding	0.00001	1/(molecule*second)	(To & Maheshri, 2010)
kOFF-rtTA-DoX-binding	0.00000002	1/second	(To & Maheshri, 2010)
kON-rtTA-DoX-geneB-binding	0.000000028	1/(molecule*second)	(Tigges et al, 2009)
kOFF-rtTA-DoX-geneB-binding	0.00001	1/second	(Tigges et al, 2009)

k-rtTA-degr	0.000096667	1/second	(Tigges et al, 2009)
k-DoX-rtTA-degr	0.000096667	1/second	(Tigges et al, 2009)
k-geneB-to-mRNAamCyan	0.0467	1/second	(Tigges et al, 2009)
k-mRNAamCyan-to-amCyan	0.00033333	1/second	(Tigges et al, 2009;Tigges et al, 2010)
k-amCyan-degr	0.000096667	1/second	(Tigges et al, 2009)

1.2. "Noisy" simulations

In order to account for the copy-number (*i.e.*, extrinsic) variability we measured experimentally the output distribution (Supplementary Figure 1C) of a transiently-transfected plasmid encoding a ZsGreen1 fluorescent protein. The amplitude of the measured fluorescence was arbitrarily assigned to correspond to 100 plasmid copies and the distribution was rescaled in copy-number units assuming linear relationship between the fluorescence and the copy-number. Plasmid copy-number was then picked randomly from that distribution (Supplementary Figure 1D) and used as an initial condition for each code execution. Furthermore, we used control experiments to estimate intrinsic variability in our circuits. The scontrol constructs (Supplementary Figures 1E, 3F) were transfected using 500 ng of the plasmid in the presence of 1000 ng/mL Dox and the fluorescence measured after 48h. The data was processed as usual (Supplementary Figures 2A-D) to generate the coefficient of variations for the individual bins. The CV of the bidirectional promoter was found to be is ~ 0.25 and the IRES junction ~ 0.30 (Supplementary Figure 1H). Next, we produced normal distributions (Supplementary Figures 1I, 1J) with zero mean and

standard deviation equaling 25% of 0.0467 sec^{-1} (the parameter values representing transcription rate from the bidirectional promoter used in simulations), and zero mean and standard deviation equaling 30% of 0.00033 sec^{-1} (the parameter values representing baseline translation rate). These distributions served to provide absolute perturbations of the original parameter values. Specifically, for each single-cell simulation, the baseline kinetic parameters are perturbed from their original values (k_{TRE}=0.0467 sec^{-1} and k_{IRES}=0.00033 sec^{-1}) by adding noise: $\mathbf{k_{TRE}=0.0467+\xi_1}$ and $\mathbf{k_{IRES}=0.00033+\xi_2}$. The "noisy" parameters ξ_1 and ξ_2 are selected randomly from the normal distributions described previously.

2. Data normalization

The data illustrated in Figures 3, 4, and 5 are normalized prior to processing in order to facilitate comparison between different circuits. (Note that the data in the supplemental material are not normalized.) As shown in Supplementary Figure 3G we use the flow cytometry scatter plots obtained with the negative control circuit of the transcriptional I1-FFL as the baseline to which we normalize the negative control data of the other motifs by making sure that the 99th percentiles of both the input and output values in the negative control measurements overlap. The normalization coefficients are shown in the table below. The resulting normalized negative controls are shown in Supplementary Figure 3H.

Motif	Multiplier X	Multiplier Y
tI1-FFL	1	1
ptI1-FFL$_I$	2.535275	2.846414
ptI1-FFL$_{II}$	1.361198	5.301537
tAM	0.653887	1.911177

3. Fitting of input-output response curves

The fitting was performed with the "Ezyfit" toolbox for Matlab, which enables curve fitting of one-dimensional data using arbitrary (non-linear) fitting functions. The results of Ezyfit, were verified using the nlitfit function in MATLAB prompt (nlinfit estimates the coefficient of a nonlinear regression using least squares estimation).

4. Fitting of input-output response curves

The coefficient of variation were fitted when necessary for illustration using the polyfit function in MATLAB, which finds the coefficients of a polynomial p(x) of degree 3 that fits the data.

5. ODE-based analytical treatment

1 Transcriptional incoherent feedforward motif model

The set of ordinary differential equations that correspond to the Type I incoherent feedforward implementation of Fig. 1a, is as follows.

$$
\begin{aligned}
\frac{dmRNAred}{dt} &= c_1 A^* - c_2 mRNAred \\
\frac{dred}{dt} &= c_3 mRNAred - c_4 red \\
\frac{dmRNALacI}{dt} &= c_8 B^* - c_5 mRNALacI \\
\frac{dLacI\_gA}{dt} &= -c_6 LacI\_gA + c_7 gA \cdot Lac4 \\
\frac{dgA}{dt} &= c_6 LacI\_gA - c_7 gA \cdot Lac4 - c_{10} DT \cdot gA + c_{11} A^* \\
\frac{dgreen}{dt} &= c_{12} mRNALacI - c_{13} green \\
\frac{dDT}{dt} &= c_{16} D \cdot tTA - c_{17} DT - c_{18} DT \cdot gB + c_{19} B^* - c_{10} DT \cdot gA + c_{11} A^* \\
\frac{dtTA}{dt} &= -c_{14} tTA + +c_{15} mRNAtta - c_{16} D \cdot tTA + c_{17} DT \\
\frac{dB^*}{dt} &= c_{18} DT \cdot gB - c_{19} B^* \\
\frac{dmRNAtta}{dt} &= stable - c_{20} mRNAtta \\
\frac{dgB}{dt} &= c_{19} B^* - c_{18} DT \cdot gB \\
\frac{dD}{dt} &= -c_{16} D \cdot tTA + c_{17} DT \\
\frac{dA^*}{dt} &= c_{10} DT \cdot gA - c_{11} A^* \\
\frac{dLacI}{dt} &= -\delta_L \cdot LacI + c_9 mRNALacI - 2 \cdot k_d \cdot (LacI)^2 + 2 \cdot k_u \cdot Lac2 \\
\frac{dLac4}{dt} &= c_6 LacI\_gA - c_7 gA \cdot Lac4 - \delta_{L4} \cdot Lac4 + k_{d2} \cdot (Lac2)^2 - k_{d4} \cdot Lac4 \\
\frac{dLac2}{dt} &= k_d \cdot (LacI)^2 - k_u \cdot Lac2 - 2 \cdot k_{d2} \cdot (Lac2)^2 + 2 \cdot k_{d4} \cdot Lac4 - \delta_{L2} \cdot Lac2
\end{aligned}
$$

The variables and constants in the system are as follows:

$stable$ = TETcells

δ_L = degradation rate of LacI monomer

δ_{L2} = degradation rate of LacI dimmer

δ_{L4} = degradation rate of LacI tetramer

k_d = dimmerization rate of LacI

k_u = dissociation rate of LacI dimmer

k_{d2} = dimmerization rate of LacI dimmer

k_{d4} = dissociation rate of LacI tetramer

$mRNAred$ = mRNAdsRed

red = dsRed

$mRNALacI$ = mRNALacI_IRES_mRNAzsGreen1

$LacI\_gA$ = LacI_geneA

gA = geneA

$green$ = zsGreen1

$mRNAtta$ = mRNArTTA

DT = DoX_tTA

tTA = tTA

B^* = tTA_DoX_geneB (active gene B)

gB = geneB

D = DoX

A^* = tTA_DoX_geneA (active gene A)

$LacI$ = LacI

$Lac4$ = LacItetramer

$Lac2$ = LacIdimer

c_i's are assorted association and dissociation and degradation/dilution rates

2 Steady states

We now solve for steady states of this system, by setting the right-hand side of the ODE to zero. For notational simplicity, we will write "$a \propto b$" to mean that there is some positive constant k (which depends only on the parameters defining the system) such that $a = kb$.

From the equations for $mRNAred$ and red we have that

$$red \propto A^*$$

and from the equation for $mRNALacI$ that

$$mRNALacI \propto B^*$$

and from the equation for $green$ that $green \propto mRNALacI$ and therefore

$$green \propto B^*$$

as well.

From the equation for free Dox, D, we have that $-c_{16}D \cdot tTA + c_{17}DT = 0$, and when this is substituted into the equation for tTA we obtain that $-c_{14}tTA + c_{15}mRNAtta = 0$, and hence, together with $mRNAtta \propto stable$, which follows from the equation for $mRNAtta$, it follows that

$$tTA = \gamma$$

where γ is some positive constant proportional to $stable$.

Hence, $-c_{16}D \cdot tTA + c_{17}DT = 0$ reduces to $-c_{16}D \cdot \gamma + c_{17}DT = 0$, from which we conclude that

$$DT \propto D\,.$$

The equations for B^* or gB give that $B^* \propto DT \cdot gB$, and the equation for A^* gives that $A^* \propto DT \cdot gA$, which since $DT \propto D$, can be also written as

$$B^* \propto D \cdot gB$$

and

$$A^* \propto D \cdot gA$$

respectively.

Also, substituting $c_{10}DT \cdot gA - c_{11}A^* = 0$ allows simplifying the equation for gA to: $c_6 LacI\_gA - c_7 gA \cdot Lac4 = 0$, which gives

$$LacI\_gA \propto gA \cdot Lac4$$

and also allows simplifying the equation obtained from the rate of $Lac4$ to

$$\delta_{L4} \cdot Lac4 + k_{d2} \cdot (Lac2)^2 - k_{d4} \cdot Lac4 = 0$$

(note that the equations for DT, $LacI\_gA$, and gA provide no additional information; they are automatically satisfied because of stoichiometry).

Letting

$$x = red \quad \text{and} \quad y = green$$

we can summarize the constraints as follows:

$$\begin{aligned} y &\propto D \cdot gA \\ x &\propto D \cdot gB \\ mRNALacI &\propto D \cdot gB \propto x \\ LacI\_gA &\propto gA \cdot Lac4 \end{aligned}$$

together with:

$$\begin{aligned} -\delta_L \cdot LacI + c_9 x - 2 \cdot k_d \cdot (LacI)^2 + 2 \cdot k_u \cdot Lac2 &= 0 \\ k_d \cdot (LacI)^2 - k_u \cdot Lac2 - 2 \cdot k_{d2} \cdot (Lac2)^2 + 2 \cdot k_{d4} \cdot Lac4 - \delta_{L2} \cdot Lac2 &= 0 \\ -\delta_{L4} \cdot Lac4 + k_{d2} \cdot (Lac2)^2 - k_{d4} \cdot Lac4 &= 0 \end{aligned}$$

where c_9 has been redefined to account for the proportionality $mRNALacI \propto x$. The last of these equations can be solved for $Lac4$ as a constant multiple of $(Lac2)^2$. The middle equation, once this is substituted, becomes a quadratic equation of the type

$$-Ku^2 - bu + cv^2 = 0$$

relating $v = LacI$ and $u = Lac2$, where b and c are positive constants and

$$K = 1 - \frac{k_{d4}}{\delta_{L4} + k_{d4}} > 0\,.$$

Since $f(u) = -Ku^2 - bu + cv^2$ is an inverted parabola with $f(0) = cv^2 > 0$, there is a unique positive solution

$$\theta(v) = \frac{-b + \sqrt{b^2 + 4cv^2}}{2K}$$

for each v, and this solution is an increasing function of v. So $Lac2 = \theta(LacI)$ may be substituted into the first equation:

$$-\delta_L v + c_9 x - 2k_d v^2 + 2k_u \theta(v) = 0 \tag{1}$$

to give a relation between x and $v = LacI$.

Two special cases are especially interesting.

Case I: Irreversible dimmerizations, low degradation

Suppose that dimmerizations are irreversible, in the sense that $k_{d4} \approx 0$ and $k_u \approx 0$ and that degradations of non-tetramer forms are very slow: $\delta_{L2} \approx 0$ and $\delta_L \approx 0$. In this case, $K = 1$ and $b = 0$, and $\theta(v) = \sqrt{c}v$, and Equation (1) says that $x \propto (Lac2)^2$. Since $Lac4$ is a constant multiple of $(Lac2)^2$, we conclude that

$$Lac4 \propto x\,. \tag{2}$$

Case II: Biphasic behavior

A qualitatively very different situation arises if the following conditions hold: $\delta_{L2} \approx 0$ and $\delta_{L4} \approx 0$ Then, the equations for the LacI forms reduce to:

$$\begin{aligned} -\delta_L \cdot LacI + c_9 x &= 0 \\ k_d \cdot (LacI)^2 - k_u \cdot Lac2 &= 0 \\ k_{d2} \cdot (Lac2)^2 - k_{d4} \cdot Lac4 &= 0 \end{aligned}$$

which implies that

$$Lac4 \propto x^4\,. \tag{3}$$

To finalize the study of steady states, we must use the fact that steady states are not be unique, as there are conserved quantities. The total amounts of gene A and gene B, in bound and unbound form, each should equal the plasmid copy number "u":

$$\begin{aligned} gA + A^* + LacI\_gA &= u \\ gB + B^* &= u \end{aligned}$$

Since also $B^* \propto D \cdot gB \propto x$ and $A^* \propto D \cdot gA \propto y$, we write $gA = \beta\frac{y}{D}$, $gB = \alpha\frac{x}{D}$ for some positive constants α and β, we can also write these gene conservation equations as follows:

$$\begin{aligned} \beta\frac{y}{D} + \gamma y + \rho\frac{y}{D} \cdot Lac4 &= u \\ \left(\frac{\alpha}{D} + \mu\right) x &= u \end{aligned}$$

for some ρ, from which we have

$$\beta\frac{y}{D} + \gamma y + \rho\frac{y}{D} \cdot Lac4 = \left(\frac{\alpha}{D} + \mu\right) x\,. \tag{4}$$

Observe that the strength of repression by LacI on the promoter of gene A is represented by the kinetic constant c_7 in the equation for $LacI\_gA$, and hence appears by the constant of proportionality in $LacI\_gA \propto gA \cdot Lac4$, which is then absorbed into ρ.

Saturated response

In the special Case I discussed above, which leads to (2), Equation (4 gives (after redefinining ρ by multiplying by a positive constant):

$$\beta\frac{y}{D} + \gamma y + \rho\frac{y}{D}x = \left(\frac{\alpha}{D} + \mu\right) x \tag{5}$$

and, if D can be assumed to be approximately constant, provides the following *Michaelis-Menten* form for y (dsRed) as a function of x (green):

$$y = \frac{Vx}{1 + kx} \tag{6}$$

for appropriate positive constants V and K. *The constant k is directly proportional, to the strength of LacI repression.* Observe that, in the unrepressed case, y is simply proportional to x.

The assumption that D, free Dox, is a constant (meaning, it is independent of copy number) is reasonable provided that initial Dox is in abundance. We analyze the effect of this approximation below.

Noise in fluorescence experimental data, as well as autofluorescence, may be modeled by additive noise in both x and y measurements. This can be accounted for by modifying the above formula to the more general form $y = \frac{Vx+W}{1+kx}$. A different parametrization of this last formula:

$$y = \sigma(x) = c\frac{x + a}{x + b} \tag{7}$$

is slightly more convenient for fitting.

Biphasic response

In the special Case II discussed above, which leads to (3), Equation (4 gives (after redefinining ρ by multiplying by a positive constant):

$$\beta\frac{y}{D}+\gamma y+\rho\frac{y}{D}x^4=\left(\frac{\alpha}{D}+\mu\right)x \tag{8}$$

and, if D can be assumed to be approximately constant, provides the following form for y (dsRed) as a function of x (green):

$$y=\frac{Vx}{1+kx^4} \tag{9}$$

for appropriate positive constants V and K. Note that this function increses from zero to some maximal value and then decreases to zero. In that sense, it is "biphasic". Once again, the assumption that D is constant is reasonable provided that initial Dox is in abundance. In any event, we show below the biphasic behavior by simulations on the full model, not assuming that D is constant.

Analysis of assumption that D is constant

The amount of free Dox "D" is in fact dependent on plasmid copy number. To study how this affects results, we use a second conservation law as well, the one that ties Dox in all its forms, bound and unbound:

$$DT+A^*+B^*+D=d_0$$

where d_0 is total initial Dox. Since $x\propto B^*$, $y\propto A^*$, and $DT\propto D$, we can rewrite this as $D+ax+by=d_0$ for some constants a and b (redefining d_0 by constant multiple).

In the case of a saturated response (the biphasic case is similar), this means that we must consider these two equations:

$$\begin{aligned}\beta\frac{y}{D}+\gamma y+\rho\frac{y}{D}x &= \left(\frac{\alpha}{D}+\mu\right)x\\ D+ax+by &= d_0\end{aligned}$$

and eliminate D in order to obtain y as a function of x that is obtained by solving a quadratic equation for y. This can be done with a symbolic computation package. To illustrate, let us pick all constants equal to 1. The solution of

$$\begin{aligned}\frac{y}{D}+y+\frac{y}{D}x &= \left(\frac{1}{D}+1\right)x\\ D+x+y &= 1\end{aligned}$$

that satisfies that $x\leq 1$ ($D+x+y\leq 1$ must be satisfied by all values) is

$$f(x)=1+\frac{1}{2}x-\frac{1}{2}\sqrt{4-4x+5x^2}\,.$$

This function increases for $x<4/5$ and decreases for $x>4/5$. On the interval $[4/5,1]$ the function is always >0.38. This means that $x+f(x)>1$ for $x>4/5$. Thus, on the domain where $D+x+y\leq 1$, the function is increasing and has a "saturating" character, as in the high-D approximation.

3 A simulation

We illustrate biphasic behavior by simulation of the full system (without making the "high D" approximation). Merely for mathematical illustration, all constants are taken equal to one, except for $\delta_{L2} = 0$ and $\delta_{L4} = 0$. Ignoring units, we take the initial amount of D to be $d_0 = 10$, and of gA and gB as u, where u is thought of as a parameter that is proportional to plasmid concentration. The constant *stable* is set to 1. All other initial conditions are set to zero. Figure S6A shows results of simulation runs that used values of u from 0.1 to 20 in steps of 0.1. The biphasic behavior is also observed for the concentrations of *red* and *green* as a function of time, as shown in Figure S6B for the case $u = 20$.

4 Post-transcriptional type 1 incoherent feedforward motif model

We next analyze mathematically a simplified model of the post-transcriptional type 1 incoherent feedforward motif. For simplicity of exposition, we omit a few of the intermediate steps from the full computational model, but a more detailed analysis, analogously to what was that done for the transcriptional incoherent feedforward motif model, could be carried out as well.

We use these species (upper case for species, lower case for concentrations):

M = mRNA (protein is in steady state proportional to M, so is omitted from the model); we also denote the concentration of M as "y" to indicate its role as output variable.

A = gene; this is the input, and will also be called "x".

B = miRNA.

P = RISC.

B^* = activated miRNA (complex BP).

Q = complex of activated miRNA and RISC (QB^*).

The simplified reactions are as follows:

$$A \xrightarrow{c_1} M + B$$

$$B + P \underset{c_3}{\overset{c_2}{\rightleftarrows}} B^*$$

$$B^* + M \xrightarrow{c_4} Q$$

$$M \xrightarrow{c_5} 0$$

$$B \xrightarrow{c_6} 0$$

$$Q \xrightarrow{c_7} B^*$$

which lead to the following differential equations:

$$\begin{aligned}
\frac{dm}{dt} &= c_1 a - c_4 b^* m - c_5 m \\
\frac{db}{dt} &= c_1 a - c_2 bp + c_3 b^* - c_6 b \\
\frac{db^*}{dt} &= c_2 bp - c_3 b^* - c_4 b^* m + c_7 q \\
\frac{dq}{dt} &= c_4 b^* m - c_7 q \\
\frac{dp}{dt} &= -c_2 bp + c_3 b^*
\end{aligned}$$

together with the conservation law for total RISC:

$$p + b^* + q \equiv c$$

where c is some positive constant. At steady state, from $\frac{dm}{dt} = 0$ we obtain:

$$m = \frac{c_1 a}{c_5 + c_4 b^*}, \tag{10}$$

from $\frac{p(b+b^*+q)}{dt} = 0$ we obtain:

$$b = \frac{c_1}{c_6} a, \tag{11}$$

from $\frac{db}{dt} = 0$ and using (11):

$$b^* = \frac{c_2}{c_3} bp = \frac{c_1 c_2}{c_3 c_6} ap, \tag{12}$$

and finally from $\frac{dq}{dt} = 0$:

$$q = \frac{c_4}{c_7} b^* m = \frac{c_1 c_2 c_4}{c_3 c_6 c_7} apm, \tag{13}$$

so, substituting (12)-(13) in the conservation law, we have also:

$$p \left[1 + \left(\frac{c_1 c_2}{c_3 c_6} + \frac{c_1 c_2 c_4}{c_3 c_6 c_7} m \right) a \right] = c. \tag{14}$$

Substituting (12) in (10), we conclude that:

$$y = \frac{Vx}{K + px} \tag{15}$$

and that p is related to x and y via (14), which we write as:

$$p\,[1 + [r + sy]x] = C, \tag{16}$$

where we have defined:

$$V = \frac{c_3}{c_4},\ K = \frac{c_3 c_5}{c_1 c_4},\ r = \frac{c_1 c_2}{c_3 c_6 c_7},\ s = r \frac{c_4}{c_7}.$$

Note that, given any V, K, r, s, one can always find c_i's such that these formulas hold (pick c_1, c_4, c_6 arbitrary and then $c_3 = Vc_4$, $c_2 = \frac{rVc_4c_6}{c_1}$, $c_5 = \frac{Kc_1}{V}$, $c_7 = \frac{r}{s}c_4$), so that the general case is captured by these new constants.

We next perform an approximate analysis, assuming that $C \gg 1$ (total RISC is very large).

For small values of x, we have that y should also be small, and thus (16) is approximated by $p = C$, which means that (15) is approximately:

$$y = \frac{Vx}{K + Cx},$$

which is a saturation function.

On the other hand, consider the behavior when x is large. Using that for large x, px is approximately $\frac{C}{r+sy}$, it follows that px is bounded, and it goes to zero provided that $y \to \infty$. So, in (15), we have that y becomes approximately equal to the linear function $\frac{V}{K}x$ provided that $y \to \infty$ (because $px \to 0$), and is in any case of linear growth.

Actually, it is always the case that $y \to \infty$. Indeed, from:

$$p\,[1 + [r + sy]x] \;=\; C$$

we have that:

$$p\,x \;=\; \frac{C}{1/x + (r + sy)} \;<\; C/r\,,$$

and therefore:

$$y \;=\; \frac{Vx}{K + px} \;>\; k\,x\,,$$

where

$$k \;=\; \frac{V}{K + C/r}\,,$$

which proves that $y \to \infty$, as claimed.

We verify these conclusions (without the approximation) with a plot of $y = y(x)$ obtained by numerically solving for p in (16), substituting in (15), and taking the positive root of the resulting quadratic equation. We pick for simplicity all constants $c_i = 1$, and total RISC $c = 1000$. We expect a behavior $y = \frac{x}{1+1000x}$, which saturates at $y = 0.001$ for small x, and asymptotically a linear behavior asymptotically with slope 1 for large x. The latter is clearly seen in Figure S6C. To appreciate the former, we zoom into the initial part of the above plot in Figure S6D.

To help visualize the two regimes, Figure S6E provides a a plot of the derivative dy/dx. Note the initial slope near zero (adaptation behavior) and final slope near 1 (linear behavior) .

6. DNA sequences of structural features

LacO sequence variants

Type	Sequence
Wild type	CGGTCTAGGTTGTGGAATTGTGAGCGCTCACAATTCTAGGTTGTGGAATTGTGAGCGCTCACAATTA
1st mutant	CCGGTCTAGGTTGTGAATTGTGAGCGGATAACAATTCTAGGTTGTGAATTGTGAGCGGATAACAATTA
2nd mutant	CCGGTCTAGGTTGTGAATTGTGACCGGATAACAATTCTAGGTTGTGAATTGTGACCGGATAACAATTA
3rd mutant	CCGGTCTAGGTTGTGAATTGTGAGGGGATAACAATTCTAGGTTGTGAATTGTGAGGGGATAACAATTA
4th mutant	CCGGTCTAGGTTGTGAATTGTAAGCGGATAACAATTCTAGGTTGTGAATTGTAAGCGGATAACAATTA
Negative Control	CCGGTCTAGGTTGTGTAGACTGAGACGTGGAGATCTCTAGGTTGTGTAGACTGAGACGTGGAGATCTA

RNAi target sequence

Type	Sequence
FF3	TTTGTATTCAGCCCATATCGTT

7. Summary of experimental conditions

DNA constructs used to implement the motifs

tI1-FFL-Wild Type	pTRE-Tight-BI-LacI-IRES-ZsGreen1-LacO-DsRed
tI1-FFL-Mutant 1	pTRE-Tight-BI-LacI-IRES-ZsGreen1-$LacO_{1st\ mt}$-DsRed
tI1-FFL-Mutant 2	pTRE-Tight-BI-LacI-IRES-ZsGreen1-$LacO_{2nd\ mt}$ -DsRed
tI1-FFL-Mutant 3	pTRE-Tight-BI-LacI-IRES-ZsGreen1-$LacO_{3rd\ mt}$ -DsRed
tI1-FFL-Mutant 4	pTRE-Tight-BI-LacI-IRES-ZsGreen1-$LacO_{4th\ mt}$ -DsRed
tI1-FFL-NegCon	pTRE-Tight-BI-LacI-IRES-ZsGreen1-$LacO_{NegCtrl}$ -DsRed
ptI1- FFL_I Wild Type	pTRE-Tight-BI-DsRed-miR-F3-AmCyan-F3

ptI1- FFL_{II} Wild Type	pTRE-Tight-BI-DsRed-miR-FF3/tgt-FF3-AmCyan
ptI1-$FFL_{I/II}$ NegCon	pTRE-Tight-BI-DsRed-miR-FF3-AmCyan-FF4x3
tAM-1xLacO	pTRE-Tight-BI-1xLacO-LacI-IRES-ZsGreen1-DsRed
tAM-2xLacO	pTRE-Tight-BI-2xLacO-LacI-IRES-ZsGreen1-DsRed
tAM-NegCtrl	pTRE-Tight-BI-2xLacO-LacI-IRES-ZsGreen1-DsRed with 1 M IPTG

Experiments shown in Figure 3

Motif	Reagent	Wait time	Plasmid Amount	Dox
tI1-FFL-Wild Type	LipoLTX	48h	500 ng	1000 ng/ml
tI1-FFL-Mutant 1	LipoLTX	48h	500 ng	1000 ng/ml
tI1-FFL-Mutant 2	LipoLTX	48h	500 ng	1000 ng/ml
tI1-FFL-Mutant 3	LipoLTX	48h	500 ng	1000 ng/ml
tI1-FFL-Mutant 4	LipoLTX	48h	500 ng	1000 ng/ml
tI1-FFL-NegCon	LipoLTX	48h	500 ng	1000 ng/ml

Experiments shown in Figure 4

Motif	Reagent	Wait time	Plasmid Amount	Dox
ptI1- FFL_{I} Wild Type	LipoLTX	48 h	500 ng	1000 ng/ml
ptI1- FFL_{II} Wild Type	LipoLTX	48 h	500 ng	1000 ng/ml

ptI1- $FFL_{I/II}$ NegCon	LipoLTX	48 h	500 ng	1000 ng/ml

Experiments shown in Figure 5

Motif	Reagent	Wait time	Plasmid Amount	Dox
tAM-1xLacO	LipoLTX	48 h	500 ng	1000 ng/ml
tAM-2xLacO	LipoLTX	48 h	500 ng	1000 ng/ml
tAM-NegCtrl	LipoLTX	48 h	500 ng	1000 ng/ml

Primers used for cloning purposes

Primer P1	CCAACGCGTCCACCATGGCCCTGTC
Primer P2	CCAGCTAGCTTATCCGGAGAAGGGCACCA
Primer P3	ACATATTTGAATGTATTTAGAAAAAT
Primer P4	AGTGAGCGAGGAAGCTCGGGGCAG
Primer P5	GTTGTCCATGGTGGCGAGACCGGTTGG
Primer P6	CCATCTAGATTACTACTGGGAGCCGGAGTG
Primer P7	CTGCAGCTTGGCGGTCTGG
Primer P8	CCAGCTAGCTTACGCTTACAATTTACGCGTTAAGATAC
Primer P9	CCAGCCGGGCCTCCCACCATGAAACCAG
Primer P10	CGAATTCTGCAGTCGACGGTAC
Primer P11	CCAGGATCCTCAGGGCAAGGCGGA
Primer P12	CTGGAGATATCGTCGACAAGC
Primer P13	AGTGAGCGAGGAAGCTCGGGGCAG
Primer P14	ACATATTTGAATGTATTTAGAAAAAT
Primer P15	CCTCGCCCTCGATCTCGAAGTA
Primer P16	CCGTCAGATCGCCTGGAGAA
Primer P17	CCTCGCCCTCGATCTCGAAGTA

Primer P18	CCAGCTAGCCCTCCCACCATGAAACCAG
Primer P19	CCAGAATTCTTACGCTTACAATTTACGCGTTAAGATAC
Primer P20	CATGACCTTATGGGACTTTCCTAC
Primer P21	TACGCGTTAAGATACATTGATGAG
Primer P22	CGTCAATGGGAGTTTGTTTTG
Primer P23	GCTGGCATAAATATCTCACTCG
Primer P24	CCAGCTAGCCTCGCCACCATGGACAAC
Primer P25	CACCCGGGCTACTGGGAGCCGGAGTG
Primer P26	GGGACTTTCCAAAATGTCGTAAC
Primer P27	CCACCCGGGCGAGCTCGAAATCTCCAGGC
Primer P28	CCAGATATCCGAGACCGGTCTAGGTTGTG
Primer P29	CCTCGCCCTCGATCTCGAAGTA
Primer P30	CCAGATATCCGAGACCGGTCTAGGTTGTG
Primer P31	GCCTTTCTTGTTCCGGTGTTAAAAACGCCACCATGGCCCTGTC
Primer P32	TTGTCTCTTGCTGGTGTTCGAAAAACGCTTACAATTTACGCGTTAAGATAC
Primer P33	AACACCGGAACAAGAAAGGCTTTTGCAGGTGGCCCCCGCGGCATATGAC
Primer P34	CGAACACCAGCAAGAGACAATTTTGCAGGTGGACGTCAGGTGGCACTTTTCG
Primer P35	CCACGGCCGGAAGCTTGTTAAGCTCGAGATCTGA
Primer P36	CCACGGCCGAGGATCCACCGGATCTAGATAACTG
Primer P37	CACTTACATATGTCAGATCCGCTAGCGCTAC
Primer P38	CTACAACATATGTTATCGAGATCTGAGTCCGGAGAA
Primer P39	CAACTGCTTCGAGCACAAGT
Primer P40	ACATTTCCCCGAAAAGTGC
Primer P41	ATCAGCCTGAAGGGCAACTG
Primer P42	CTGAGTCCGGAGAAGGGCAC
Primer P43	GCCACCACCTGTTCCTGAGATC
Primer P44	TTATCTAGATCCGGTGGATCCC
Primer P45	GCGTGATGAACTTCGAGGAC

Oligos used for cloning purposes

Oligo O1	CCGGTCTAGGTTGTGGAATTGTGAGCGCTCACAATTCTAGGTTGTGGAATTGTGAGCGCTCACAATTA
Oligo O2	CCGGTAATTGTGAGCGCTCACAATTCCACAACCTAGAATTGTGAGCGCTCACAATTCCACAACCTAGA
Oligo O3	GGCCGCCGCTTGAAGTCTTTAATTAAACCGCTTGAAGTCTTTAATTAAACCGCTTGAAGTCTTTAATTAAAC
Oligo O4	GGCCGTTTAATTAAAGACTTCAAGCGGTTTAATTAAAGACTTCAAGCGGTTTAATTAAAGACTTCAAGCGGC
Oligo O5	AGCTTACTAACATGCTTCGAAACGATATGGGCTGAATACAAAG
Oligo O6	TCGACTTTGTATTCAGCCCATATCGTTTCGAAGCATGTTAGTA

siRNAs used targeting AmCyan

siRNA-1	GCCACUACUUCACCGUGAAUU **GCCGGUGAUGAAGUGGCACUU**
siRNA-7	CCUCCUACAAGACCAAGAAUU **GUGGAGGAUGUUCUGGUUCUU**

8. DNA Plasmids

pTRE-Tight-BI-AmCyan-DsRed: AmCyan gene was amplified from the AmCyan-C1 plasmid (Clontech) using primers P1 and P2 with NheI and MluI restriction sites. The product was digested with NheI and MluI and repurified. In parallel, pTRE-Tight-BI (Clontech) was digested with NheI and MluI and gel-purified. The digested insert was ligated into the digested vector at 1:2 ratio at 12 ^{o}C overnight, transformed and expanded. The construct was sequenced using primers P3 and P4. The DsRed-monomer gene was amplified from the pCAGOP-DsRed-Monomer-N1 plasmid (Rinaudo et al, 2007) using primers P5 and P6 with XbaI and AgeI restriction sites. The PCR product was digested with XbaI and AgeI enzymes. In parallel, the above pTRE-Tight-BI-AmCyan plasmid was digested with XbaI and AgeI and gel-purified. The digested DsRed-monomer insert was ligated into the digested vector at 1:1 ratio at 14 ^{o}C overnight, transformed and expanded. Correct constructs were identified by double EagII and BglII digestion and by observing fluorescence in transfected cells.

pTRE-Tight-BI-AmCyan-LacO-DsRed: pTRE-Tight-BI-AmCyan-DsRed was digested by AgeI and purified. The backbone was dephosphorylated and purified. Oligos O1 and O2 (Sigma) containing a tandem repeat of the wild type LacO sequence CTAGGTTGTGGAATTGTGAGCGCTCACAATT were gel-purified using 20% denaturing PAGE and annealed. The double-stranded LacO insert with AgeI-compatible sticky ends was phosphorylated and ligated into AgeI-digested and purified pTRE-Tight-BI-AmCyan-DsRed backbone at 1:3 ratio at 14 ^{o}C overnight. The ligation product was transformed and expanded. LacO sites integrity was verified by sequencing with P7.

pTRE-Tight-BI-LacI-LacO-DsRed: LacI gene was amplified from CMV-LacI-F3x3 (Rinaudo et al., 2007) using primers P8 and P9 with XmaI and NheI restriction sites and digested with these enzymes. In parallel, pTRE-Tight-BI-AmCyan-LacO-DsRed was digested with XmaI and NheI to remove AmCyan sequence. The digested LacI insert was ligated into the gel-purified backbone vector at 1:4 ratio at 14 ^{o}C overnight, transformed and expanded. The correct clones were verified by separate NheI and BglII digestions.

pTRE-Tight-BI-LacI-IRES-ZsGreen1-LacO-DsRed: IRES-ZsGreen1 sequence was amplified from pIRES2-ZsGreen1 (Clontech) using primers P10 and P11 with BamHI restriction sites, and digested with BamHI. In parallel, pTRE-Tight-BI-LacI-LacO-DsRed was digested with BamHI, gel-purified and dephosphorylated. The digested IRES-ZsGreen1 insert was ligated into the digested vector at 1:4 ratio at 14 ^{o}C overnight, transformed and expanded. The clones were verified by sequencing with primers P12, P13, and P14.

pTRE-Tight-BI-LacI-IRES-ZsGreen1-LacO$_X$-DsRed (X = 1st mt, 2nd mt, 3rd mt, 4th mt and NegCtrl): LacO mutant inserts with AgeI-compatible sticky ends were prepared similarly to the

wild-type LacO insert. pTRE-Tight-BI-LacI-IRES-ZsGreen1-LacO-DsRed was digested by AgeI and gel-purified. The backbone and the inserts were ligated at 1:3 ratio at room temperature for 10 minutes, transformed and plated. Colonies were analyzed by colony PCR using primers P15 and P16, positive colonies were expanded overnight, plasmid DNA was isolated and the results were verified by sequencing with primer P17.

LacI-FF3-pIRES2-ZsGreen1: LacI gene with the FF3 siRNA target in the 3'-UTR was amplified from CMV-LacI-FF3 (Rinaudo et al, 2007) using primers P18 and P19 with NheI and EcoRI restriction sites. pIRES2-ZsGreen1 vector and LacI amplicon were digested with NheI and EcoRI enzymes, and vector DNA was gel-purified and dephosphorylated. The digested backbone and insert were ligated at 1:2 ratio overnight, transformed and plated. Colonies were analyzed by colony PCR using primers P20 and P21. Positive colonies were expanded, and the clones were verified by sequencing with primers P22 and P23.

DsRed-pIRES2-ZsGreen1: DsRed-monomer gene was amplified from the pCAGOP-DsRed-Monomer-N1 plasmid (Rinaudo et al, 2007) using primers P24 and P25 with NheI and XmaI restriction sites. LacI-FF3-pIRES2-ZsGreen1 plasmid and the PCR product were digested by NheI and XmaI enzymes and gel-purified. Gel-purified backbone and insert were ligated at a 1:3 ratio at room temperature for 10 minutes, transformed, plated and expanded. Clones were verified by sequencing with primer P26.

pTRE-Tight-BI-1xLacO-LacI-IRES-ZsGreen1-DsRed and **pTRE-Tight-BI-2xLacO-LacI-IRES-ZsGreen1-DsRed**: These plasmids were constructed from pTRE-Tight-BI-LacI-IRES-ZsGreen1-LacO-DsRed by inverting the region between the LacI and the DsRed genes that contains the bidirectional promoter and the LacO sequences. The backbone vector excluding this

region was amplified using primers P27 and P28 with XmaI and EcoRV restriction sites, respectively. The PCR product was gel-purified, digested using XmaI and gel-purified once more. The backbone vector was digested with SacI (which removed the pTRE-LacO region) and purified. Digested vector was blunted with Mung Bean Nuclease, digested with AgeI and gel purified. The insert and backbone, with one side having compatible AgeI and XmaI sticky ends and the other side blunt ends, were ligated at 1:1 and 1:2 ratios at 16 ^{o}C overnight and transformed into EPI300 E. Coli (Epicentre). Plasmid DNA was sequenced with primer P29. Two separate colonies resulting from the 1:1 and 1:2 ligations respectively yielded constructs with single and double repeats of the LacO.

pTRE-Tight-BI-DsRed-miR-FF3-AmCyan-FF3: pCMV-AmCyan-FF3 was constructed by replacing ZsYellow1 in pCMV-ZsYellow1-FF3 (Rinaudo et al, 2007) with AmCyan from pAmCyan-C1 (Clontech) by using NheI and BglII. AmCyan-FF3 was amplified from pCMV-AmCyan-FF3 with primers P31 and P32, and chewed back with 1.2 U T4 polymerase in the presence of 1mM dTTP at 27 °C for 5 min. DsRed-miR-FF3 was amplified from pTRE-tight-bi-DsRed-FF3(Leisner et al, 2010) with primers P33 and P34 and chewed back with 1.2 U T4 polymerase in the presence of 1 mM dATP at 27 °C for 5 min. Chew-back reactions were stopped by heat-inactivation of T4 polymerase at 75 °C for 20 min. Then two chewed DNA fragments were annealed by gradually lowering the temperature from 75 °C to 25 °C. The product was transformed into EPI300.

pTre-Tight-BI-DsRed-miR-FF3-AmCyan (negative control for pTI1-FFL circuits): The AmCyan coding sequence from pAm-Cyan-C1 was amplified using primers P37 and P38 with NdeI sites. The PCR product and pTRE-tight-bi-DsRed-FF3 (Leisner et al, 2010) were digested with NdeI, backbone DNA was dephosphorylated, and the two were ligated at 1:3 ratio. The

construct was transformed and plated. Colonies were tested by PCR using primers P39 and P40, followed by sequencing using primers P41 and P42.

pTRE-Tight-BI-DsRed-miR-FF3/tgt-FF3-AmCyan: Synthetic FF3 sites with HindIII and SalI-compatible sticky ends were synthesized (IDT) by annealing and phosphorylating O5 and O6. pTre-Tight-BI-DsRed-FF3-AmCyan backbone was digested with HindIII and SalI and subsequently ligated with the synthetic insert. Constructs were transformed and plated. Colonies were tested using primers P43 and P44, expanded and sequenced using primer P45.

9. Cloning kits

PCR product purifications were performed using the Qiagen PCR purification kit. Gel-purifications were performed using Qiagen Gel Purification kit from 1% agarose gel. DNA isolations were performed using Qiagen MiniPrep kit. Sequencing was performed by Genewiz.

Supplemental References

Hsieh M, Brenowitz M (1997) Comparison of the DNA Association Kinetics of the Lac Repressor Tetramer, Its Dimeric Mutant LacI adi , and the Native Dimeric Gal Repressor. *Journal of Biological Chemistry* **272:**22092-22096.

Leisner M, Bleris LG, Lohmueller J, Xie Z, Benenson Y (2010) Rationally designed logic integration of regulatory signals in mammalian cells. *Nature Nanotechnology* **5:** 666-670

Ozbudak EM, Thattai M, Lim HN, Shraiman BI, Van Oudenaarden A (2004) Multistability in the lactose utilization network of Escherichia coli. *Nature* **427:**737-740

Rinaudo K, Bleris LG, Maddamsetti R, Subramanian S, Weiss R, Benenson Y (2007) A universal RNAi-based logic evaluator that operates in mammalian cells. *Nature Biotechnology* **25:**795-801

Tigges M, Marquez-Lago T, Stelling J, Fussenegger M (2009) A tunable synthetic mammalian oscillator. *Nature* **457:**309

Tigges M, Dénervaud N, Greber D, Stelling J, Fussenegger M (2010) A synthetic low-frequency mammalian oscillator. *Nucleic Acids Research* **38:**2702-2711

To T, Maheshri N (2010) Noise Can Induce Bimodality in Positive Transcriptional Feedback Loops Without Bistability. *Science* **327:**1142-1145